Center for Photonics and Quantum Materials,
Skolkovo Institute of Science and technology

Department of Applied Physics,
Aalto University

Enhancing Optoelectronic Performance of Randomly Oriented Single-Walled Carbon Nanotube Films

Alexey P. Tsapenko

Skoltech
Skolkovo Institute of Science and Technology

Aalto University

DOCTORAL DISSERTATIONS

Skoltech
Skolkovo Institute of Science and Technology

Skolkovo Institute of Science and Technology / Doctoral Program in Physics
DOCTORAL THESIS

Enhancing Optoelectronic Performance of Randomly Oriented Single-Walled Carbon Nanotube Films

Alexey P. Tsapenko

Supervisors:	Professor Albert G. Nasibulin, Skolkovo Institute of Science and Technology, Russia
	Professor Esko I. Kauppinen, Aalto University, Finland
Defense Jury:	Professor Nikolay A. Gippius (Chairman), Skolkovo Institute of Science and Technology, Russia
	Assistant Professor Toma Susi, University of Vienna, Austria
	Professor Krisztian Kordas, University of Oulu, Finland
	Professor Georgy E. Fedorov, Moscow Institute of Physics and Technology, Russia
	Professor Sergey D. Shandakov, Kemerovo State University, Russia
	Professor Alexander V. Okotrub, Novosibirsk State University, Russia
Date & Time:	October 4, 10:30
Venue:	Skolkovo Institute of Science and Technology, 30, Bolshoi Boulevard, bld. 1, Room B4-3007a

© Alexey P. Tsapenko, 2019

Aalto University publication series
DOCTORAL DISSERTATIONS 176/2019

Enhancing Optoelectronic Performance of Randomly Oriented Single-Walled Carbon Nanotube Films

Alexey P. Tsapenko

A doctoral dissertation conducted under a convention for the joint supervision of thesis at Aalto University (Finland) and Skolkovo Institute of Science and Technology (Russia) for the degree of Doctor of Science (Technology) at Aalto University, to be defended, with the permission of the Aalto University School of Science, at a public examination held at the lecture hall AS3 of the school on 4th October 2019 at 10:30.

Aalto University
School of Science
Department of Applied Physics

Supervising professors
Esko I. Kauppinen, Aalto University, Finland
Albert G. Nasibulin, Skolkovo Institute of Science and Technology, Russia

Preliminary examiners
Professor Krisztian Kordas, University of Oulu, Finland
Professor Alexander V. Okotrub, Novosibirsk State University, Russia

Opponent
Professor Alexander V. Okotrub, Novosibirsk State University, Russia

Aalto University publication series
DOCTORAL DISSERTATIONS 176/2019

© 2019 Alexey P. Tsapenko

ISBN 978-952-60-8737-5 (printed)
ISBN 978-952-60-8738-2 (pdf)
ISSN 1799-4934 (printed)
ISSN 1799-4942 (pdf)
http://urn.fi/URN:ISBN:978-952-60-8738-2

Unigrafia Oy
Helsinki 2019

Finland

NORDIC SWAN ECOLABEL
Printed matter
4041-0619

Aalto University

Abstract

Aalto University, P.O. Box 11000, FI-00076 Aalto www.aalto.fi

Author
Alexey P. Tsapenko

Name of the doctoral dissertation
Enhancing Optoelectronic Performance of Randomly Oriented Single-Walled Carbon Nanotube Films

Publisher School of Science

Unit Department of Applied Physics

Series Aalto University publication series DOCTORAL DISSERTATIONS 176/2019

Field of research Engineering Physics

Manuscript submitted 18 June 2019 **Date of the defence** 4 October 2019

Permission for public defence granted (date) 22 August 2019 **Language** English

☐ **Monograph** ☒ **Article dissertation** ☐ **Essay dissertation**

Abstract

Randomly oriented single-walled carbon nanotubes (SWCNTs) in the form of films are a promising material for various optoelectronic and photonic applications, including actual flexible and stretchable, transparent and conductive electrodes. However, the optoelectronic performance of as-synthesized SWCNT films still needs to be improved in order to provide industry-required conductivity characteristics.

In this thesis, several novel approaches are introduced to enhance the optoelectronic properties of the films by an adsorption doping technique. The first approach based on the creation of a hybrid graphene/SWCNT material allowed us to reduce the sheet resistance by introducing a large area π-stacking interaction between the carbon nanomaterials. The second one is devoted to the optimization of an adsorption doping technique with a correct selection of a dopant solvent in which the evaporation rate is the most important parameter to control the optoelectric properties of the SWCNT films. The final one presents an aerosol-assisted approach that focuses on a uniform, controllable, and reproducible doping which leads to fine-tuning of the SWCNT film work function and conductivity.

Additionally, the optical properties of the as-synthesized and doped nanotubes were extensively studied using broad wavelength non-destructive spectroscopies and optical pumping with a terahertz probe. The first study contributes and confirms the observable spectral effects for free carriers described in the Drude conductivity model. The second one identifies strong negative photoconductivity in both pristine and doped nanotubes.

As a result, each of these cases leads to the creation of the SWCNT films that exhibit superior properties. This opens up numerous breathtaking opportunities for today and upcoming devices.

Keywords SWCNT, TCF, optoelectronic performance, adsorption doping, fine-tuning

ISBN (printed) 978-952-60-8737-5 **ISBN (pdf)** 978-952-60-8738-2

ISSN (printed) 1799-4934 **ISSN (pdf)** 1799-4942

Location of publisher Helsinki **Location of printing** Helsinki **Year** 2019

Pages 125 **urn** http://urn.fi/URN:ISBN:978-952-60-8738-2

For Kostya and Natasha

Contents

Acknowledgements

The research work comprised in this thesis was mainly conducted between October 2014 and October 2019 in both the Laboratory of NanoMaterials (LNM) of the Center for Photonics and Quantum Materials of the Skolkovo Institute of Science and Technology (Skoltech) and the NanoMaterials Group (NMG) of the Department of the Applied Physics of Aalto University (Aalto) School of Science.

Being among the first doctoral students of LNM, I have been privileged to learn the laboratory construction from the ground up. At the same time, our joint works with the already leading experts in the field (NMG) and multiple academic (MIT, MIPT, MSU, *etc.*), as well as industrial partners (Canatu Ltd.), allowed us to build excellent resources, equipment, and a unique environment for the students. Furthermore, I have met and got acquainted with numerous persons from around the world, discussed and got insights into a wide range of previously unknown or hidden opportunities and skills.

For this magnificent chance and for the continuous support, guidance, and encouragement of my dissertation, I would like to express my deep gratitude to my supervising professors Albert G. Nasibulin and Esko I. Kauppinen. The excellent atmosphere in their research groups, closely linked to the strategic vision on the future of technologies, motivated me to fulfill all given tasks to the best of my abilities and elaborated on my own research methods and techniques. In addition, during the entire period, I always felt welcome and was treated as an equal.

Besides my supervisors, I would like to thank and recognize many other supporters. As each research require an idea and a stimulating discussion to start with, I was really happy to learn this from Dr. Ilya V. Anoshkin, Dr. Dmitri V. Lioubtchenko, Dr. Hua Jiang, professor Olli Ikkala and his group members, researchers from the Low-Temperature Laboratory of Aalto and many others in the early stage of my work. The extensive and successful experience throughout my work was, of course, made possible with fruitful criticism and comments, joint and highly-productive but sometimes long and overnight conversations with my present and former lab mates at Skoltech and Aalto. In particular, I wish to acknowledge the close collaboration and/or teamwork with Stepan A. Romanov, Daria A. Satco, Maria G. Burdanova, Alena A. Alekseeva, Pramod M. Rajanna, Sergei O. Volosheniuk, Alexandra L. Vyatskikh, Andrey Krivoy, Georgy

A. Ermolaev, Boris Yu. Zabelich, Andrey Starkov, and Dr. Anastasia E. Goldt. Dr. Dmitry V. Krasnikov, Dr. Qiang Zhang, Eldar M. Khabushev, and Vsevolod Ya. Iakovlev are saluted for their personal assistance and continuous support with the reactor construction and nanotube synthesis. My warmest thanks for the help are also extended to our collaborators, co-authors, master and doctoral students, post-doctoral researches, and engineers from the related laboratories of professors: Boris P. Gorshunov, James Lloyd-Hughes, Tanja Kallio, Nikolay A. Gippius, Keith J. Stevenson, Vladimir P. Drachev, Anvar A. Zakhidov, Sergei Bereznev, Leonid A. Chernozatonskii, Vadim M. Levin, Vitold E. Pozhar, Pavel B. Sorokin, Vitaly V. Podzorov, A. John Hart, *etc.*

The present and former members of education, public relations, human resources, administration, and legal offices of both Skoltech and Aalto deserve to be thanked for facilitating with all the practicalities and bureaucracy. I would also like to thank the jury members and pre-examiners of this thesis, who helped to improve the text with their comments and questions. I am also thankful to the opponents, for accepting the invitation to serve as the opponents.

This research has been made possible with funding from multiple sources, including the Russian Science Foundation No. 17-19-01787 (synthesis, measurements, and characterization of the thin films), the Russian Foundation for Basic Research No. 18-32-00246 (optical measurements and analysis of the samples), the Ministry of Education and Science of the Russian Federation No. RFMEFI58114X0006 (characterization of the hybrid materials), Skoltech NGP Program (Skoltech-MIT joint project), and the Finnish National Agency for Education (EDUFI fellowship).

Last but not least I would like to thank my parents and my brother for their never-ending and unconditional support, kind attitude to life and warm love. I would also like to deeply appreciative my family members and our friends from all over the world for their eternal love, supporting attitude and encouragement during complicated life situations we faced.

It is a pleasure to live and work with you.
I love you all.

Espoo, 16 September 2019
Alexey P. Tsapenko

List of abbreviations and symbols

1D	one-dimensional
3D	three-dimensional
AC	alternating current
ACN	acetonitrile
BE	binding energy
BWO	backward-wave oscillator
CNT	carbon nanotube
CVD	chemical vapour deposition
CW	continuous-wave
DC	direct current
DDQ	2,3-dichloro-5,6-dicyano-p-benzoquinone
$NOBF_4$	nitrosyl tetrafluoroborate
DOS	density of states
DFT	density-functional theory
DMF	dimethylformamide
DMSO	dimethylsulfoxide
EtOH	ethanol
eV	electron volt
ED	electron diffraction
ETB	extended tight-binding
FoM	figure of merit
FT	Fourier-transform
GMD	geometric mean diameter
GSD	geometric standard deviation

HR	high-resolution
IR	infrared
ITO	indium tin oxide
MB	many-body
NHE	normal hydrogen electrode
NIR	near-infrared
NMP	n-methyl-2-pyrrolidone
NP	nanoparticle
NSD	number size distributions
OAS	optical absorption spectroscopy
OLED	organic light-emitting diode
PEDOT:PSS	poly(3,4-ethylenedioxythiophene) polystyrene sulfonate
RBM	radial breathing mode
SEM	scanning electron microscope
SWCNT	single-walled carbon nanotube
TB	tight-binding
TCF	transparent conductive film
TD	time-domain
TEM	transmission electron microscope
THF	tetrahydrofuran
THz	terahertz
UPS	ultraviolet photoelectron spectroscopy
UV	ultraviolet
vHs	van Hove singularity
Vis	visible
XPS	X-ray photoelectron spectroscopy

Thesis publications

This doctoral dissertation consists of a summary of the following publications which are referred to in the text by their numerals:

I. **Tsapenko, A.P.**, Goldt, A.E., Shulga, E., Popov, Z.I., Maslakov, K.I., Anisimov, A.S., Sorokin, P.B. and Nasibulin, A.G., 2018. Highly conductive and transparent films of $HAuCl_4$-doped single-walled carbon nanotubes for flexible applications. Carbon, 130, pp.448-457. ISSN: 0008-6223. https://doi.org/10.1016/j.carbon.2018.01.016.

II. **Tsapenko A.P.**, Romanov S.A., Satco D.A., Krasnikov D.V., Rajanna P.M., Danilson M., Volobujeva O., Anisimov A.S., Goldt A.E., Nasibulin A.G., 2019, Aerosol-assisted fine-tuning of optoelectrical properties of SWCNT films. The Journal of Physical Chemistry Letters, 2019, 10, 14, p.3961-3965. ISSN: 1948-7185. DOI: 10.1021/acs.jpclett.9b01498.

III. Burdanova, M.G., **Tsapenko, A.P.**, Satco, D.A., Kashtiban, R.J., Mosley, C., Monti, M., Staniforth, M., Sloan, J., Gladush, Y., Nasibulin, A.G. and Lloyd-Hughes, J., 2019. Giant negative terahertz photoconductivity in controllably doped carbon nanotube networks. ACS Photonics, 2019 6 (4), 1058-1066. ISSN: 2330-4022. DOI: 10.1021/acsphotonics.9b00138.

IV. Zhukova, E.S., Grebenko, A.K., Bubis, A.V., Prokhorov, A.S., Belyanchikov, M.A., **Tsapenko, A.P.**, Gilshteyn, E.P., Kopylova, D.S., Gladush, Y.G., Anisimov, A.S. and Anzin, V.B., 2017. Terahertz-infrared electrodynamics of single-wall carbon nanotube films. Nanotechnology, 28(44), p.445204. ISSN: 0957-4484. https://doi.org/10.1088/1361-6528/aa87d1.

V. Gorkina, A.L., **Tsapenko, A.P.**, Gilshteyn, E.P., Koltsova, T.S., Larionova, T.V., Talyzin, A., Anisimov, A.S., Anoshkin, I.V., Kauppinen, E.I., Tolochko, O.V. and Nasibulin, A.G., 2016. Transparent and conductive hybrid graphene/carbon nanotube films. Carbon, 100, pp.501-507. ISSN: 0008-6223. https://doi.org/10.1016/j.carbon.2016.01.035.

Author's contribution

I. The author is mainly responsible for the work. The author conceived and conducted the experiments apart from the TEM studies and DFT calculations. The author was responsible for writing the manuscript.

II. The author is mainly responsible for the work. The author was responsible for the doping set-up design, conceiving and conducting the experimental work and data analysis. The author was responsible for writing the manuscript.

III. The author was responsible for design and implementation of the doping set-up, optical UV-Vis-NIR characterization of SWCNT films and co-author the manuscript.

IV. The author was responsible for sample preparation, doping procedure, DC measurements, Raman characterization, and collecting spectra in the UV-Vis-NIR region. THz- and IR-region measurements were conducted by co-authors. The author was also responsible for co-writing the manuscript.

V. The author was responsible for conducting the optical and electrical experiments together with co-authors and co-author the manuscript. The XPS and SEM measurements were conducted by co-authors.

Other featured publications

A. Kanninen, P., Luong, N.D., Anoshkin, I.V., **Tsapenko, A.**, Seppälä, J., Nasibulin, A.G. and Kallio, T., 2016. Transparent and flexible high-performance supercapacitors based on single-walled carbon nanotube films. Nanotechnology, 27(23), p.235403. ISSN: 0957-4484. https://doi.org/10.1088/0957-4484/27/23/235403

B. Funde, A.M., Nasibulin, A.G., Syed, H.G., Anisimov, A.S., **Tsapenko, A.**, Lund, P., Santos, J.D., Torres, I., Gandía, J.J., Cárabe, J. and Rozenberg, A.D., 2016. Carbon nanotube–amorphous silicon hybrid solar cell with improved conversion efficiency. Nanotechnology, 27(18), p.185401. ISSN: 0957-4484. https://doi.org/10.1088/0957-4484/27/18/185401.

C. Kopylova, D.S., Fedorov, F.S., Alekseeva, A.A., Gilshteyn, E.P., **Tsapenko, A.P.**, Bubis, A.V., Grebenko, A.K., Popov, Z.I., Sorokin, P.B., Gladush, Y.G. and Anisimov, A.S., 2018. Holey single-walled carbon nanotubes for ultra-fast broadband bolometers. Nanoscale, 10(39), pp.18665-18671. ISSN: 2040-3372. http://dx.doi.org/10.1039/c8nr05925j.

D. Gilshteyn, E.P., Lin, S., Kondrashov, V.A., Kopylova, D.S., **Tsapenko, A.P.**, Anisimov, A.S., Hart, A.J., Zhao, X. and Nasibulin, A.G., 2018. A one-step method of hydrogel modification by single-walled carbon nanotubes for highly stretchable and transparent electronics. ACS applied materials & interfaces, 10(33), pp.28069-28075. ISSN: 1944-8244. https://doi.org/10.1021/acsami.8b08409.

E. Zhukova, E.S., Gorshunov, B.P., **Tsapenko, A.P.**, Grebenko, A.K., Bubis, A.V., Zhukov, S.S., Simchuk, E.A., Tsebro, V.I., Tonkikh, A.A., Rybkovskiy, D.V. and Kauppinen, E.I., 2018, September. Charge transport mechanisms in macro-scale CNT films. In Journal of Physics: Conference Series (Vol. 1092, No. 1, p. 012178). IOP Publishing. ISSN: 1742-6596. https://doi.org/10.1088/1742-6596/1092/1/012178

F. Krasnikov, D.V., Zabelich, B.Y., Iakovlev, V.Y., **Tsapenko, A.P.**, Romanov, S.A., Alekseeva, A.A., Grebenko, A.K. and Nasibulin, A.G., 2019. A spark discharge generator for scalable aerosol CVD synthesis of single-walled carbon nanotubes with tailored characteristics. Chemical Engineering Journal, 372, pp.462-470, ISSN 1385-8947, https://doi.org/10.1016/j.cej.2019.04.173.

1. Introduction

Carbon nanotubes (CNTs) and especially single-walled carbon nanotubes (SWCNTs) have become a hot topic over the last two decades. Since their mentioning through Iijima's publications in a multidisciplinary journal *Nature* [1,2], this material fascinates scientists not only from a fundamental point of view [3–6] but also due to its incredible flexibility and stretchability properties suitable for numerous areas of our everyday life and in the future. Currently, among various synthesis methods, chemical vapor deposition (CVD) and aerosol CVD, in particular, is found to be a unique and highly efficient technology for large-scale production of SWCNT films with different thicknesses, nanotube length and diameter distributions [7,8]. Despite the huge progress in the field of synthesis, the development of appropriate post-synthesis modification methods and techniques remains very important.

The solar, optoelectronic, and photonic industries are considered to be among the main technological areas that will require the material in the form of a transparent and conductive film. Industries demand the homogenous SWCNT-based large-scale films to be as transparent and conductive as possible. Recently, several key market players, *e.g*. Huawei and Samsung, have released the first prototypes of foldable touch screens employing SWCNTs/conductive polymers as the anode layer [9,10]. Unlike transport layers based on brittle metal-oxides, *e.g*. indium tin oxide (ITO), currently used on virtually any screen, SWCNT-based films allow the prototypes to be bendable and foldable at least in one direction. The trend of free-form design on different surfaces will only grow as the device complexity and functionality will evolve from year to year. As a consequence, the further use of the SWCNT film is largely dependent on the enhancement of the optical and electrical characteristics of as-produced nanotubes.

To provide a solution to the low optoelectronic performance issue, this thesis focuses on modifying the widely used adsorption-doping technique. The thesis consists of two interconnected parts devoted to the main objectives of the research – the analysis of the optical parameters of the SWCNT films and the production of a highly transparent and conductive material.

The first part discusses the optical response of as-synthesized (pristine) and subsequently doped films. The work emphasizes that the optical and electronic properties of SWCNT films are unique and determined not only by specific intrinsic characteristics of the individual nanotubes but also by external film factors (alignment of nanotubes, presence of inter nanotube contacts, distribution of lengths and diameters of SWCNTs, *etc.*). Systematic measurements of broad-wavelength spectra of the real and imaginary conductance of both pristine and doped films with different thicknesses are performed to estimate the effective parameters of charge carriers (mobility, scattering rate, and mean-free path) in the films. The work explains how to control the effective parameters associated with the peak changes observed in the broad-wavelength spectra during doping.

The second part is devoted directly to the optimization and modification of the adsorption doping concept as the most efficient way to achieve high conductivity values with high transmittance in the visible range of the optical spectrum. The first approach combines the best properties of both SWCNTs and graphene to create a hybrid material. Since the conductivity of the SWCNT films is limited by the contact resistance between individual nanotubes, their performance can be significantly improved by a large area π-stacking interaction created between the carbon nanomaterials. Moreover, subsequent doping of this hybrid material ensures excellent optoelectronic characteristics. The influence of solvent parameters on the resulted optoelectronic performance of doped films is discussed in the second approach. When using this method, the evaporation rate is considered the most influential parameter, which is attributed to the correlation of the resulting film resistances with temperature-dependent parameters of used solvents. Hence, adjusting the temperature, at which the doping is done, allows to optimize the parameters for reaching superior and stable performance. The third approach based on previously optimized solution parameters aims to develop a dopant deposition technique suitable for mass-production. The method employs the aerosol-assisted approach with the nebulizer-generated tiny dopant droplets for a uniform dopant distribution over the film. Additionally, this aerosol-assisted doping allows the fine-tuning of optoelectronic characteristics including highly desirable control parameters such as work function and sheet resistance.

Finally, from the practical point of view, this thesis reveals the importance of careful control of each stage of the post-synthesis processes and introduces straightforward guidelines for reaching the state-of-the-art values of optical and electronic characteristics of SWCNT films. Moreover, it serves as a block building technique for future industrial optimization processes to establish the most important optical and electrical parameters of the SWCNT films.

2. Transparent conductive films

Transparent conductive films (TCFs) are based on the materials that possess both low electrical resistance and high optical transmittance. They are crucial, for instance: for touch screens and sensors, solar cells and organic light-emitting diode (OLED) panels, as well as for heated windscreens, *etc.*

2.1 Industry standard – Metal Oxides

Nowadays, conductive metal oxides and ITO in particular, are proven industry standard materials. This is due to the low resistivity after preparation and thermal annealing, high transmittance in the visible spectrum, environmental stability, and easy etching feasibility, *e.g.* for direct contact drawing with lithographic patterning. At the same time, ITO has some major drawbacks for modern and future devices. The brittleness and general poor mechanical properties, as well as the deterioration of ITO characteristics (*e.g.* an unpredictable increase in resistance and a change in transmittance) during applied deformation and/or distortion processes, come to the fore. This is the bottleneck of ITO applicability in flexible and stretchable electronics. Additionally, ITO possesses a high refractive index and haze. The former requires to put several more optical matching layers on top of it in order to minimize the Fresnel reflection. The latter inhibits the white light passing through the film to be vibrant. Furthermore, the production of high-quality ITO needs vacuum and heat treatment, which limits the use of transparent, flexible and stretchable polymer substrates (that usually barely withstand temperatures above $\mathrm{T} = 150\,°C$). In combination with the fact of being based on a rare-material as indium, resources of which are limited and the price of associated commodities is constantly increasing [11,12], ITO is extensively sought to be replaced with alternative materials.

2.2 Alternative TCF materials

Among the various alternative TCF materials, SWCNT- and graphene-based TCFs are the leading ones because of their intrinsic ballistic conductance nature.

However, for a wide range of applications, it is necessary at least to optimize their optoelectronic characteristics. There are other materials also modified and optimized to reach the ITO levels of an optoelectronic performance: Cu and Ag nanowires and nanofibers [13], aluminum-doped zinc oxide [14], conductive polymers such as PEDOT:PSS, graphene, *etc*. Although these alternative materials have optoelectronic characteristics that are comparable and sometimes even higher than for ITO, there are other difficulties that challenge their application. In the case of nanowires and metal-doped oxides, the problem is oxidation under ambient conditions, while quick degradation in time is the issue for PEDOT:PSS. Other conductive polymers and carbon-based materials can have better flexibility than ITO, but usually, their electrical conductivity, stability, and net stretchability limit their use [9,15]. Additionally, for graphene, it is difficult to grow single-crystal of large-area with a small number of defects. As a recent trend, hybrids and/or composites on the basis of mentioned materials have started to evolve rapidly, which finally can result in synergetic effects between the combined materials and improve the performance [16].

2.3 SWCNT films

CNTs, and especially SWCNTs, are the most promising replacement material for metal oxides in TCFs. Various treatment methods of SWCNTs have been used to demonstrate the possibilities of this material in TCFs: deposition of stabilized solutions, ultrasonic treatment, numerous post-deposition methods, and film processing. Among the lowest reproducible reported values are results of Hecht *et al.* (equivalent sheet resistance value is $R_{90} = 60\,\Omega/\square$, corresponding to the as-measured sheet resistance ($R_S = 60\,\Omega/\square$) and transmittance at $550\,nm$ ($T_{550} = 90\%$)) [17], Anoshkin *et al.* (reached $R_{90} = 73\,\Omega/\square$ for aerosol CVD nanotubes grown from ethylene and treated with gold (III) chloride ($AuCl_3$)) [18], Nasibulin *et al.* and Kaskela *et al.* (reported R_{90} of $84\,\Omega/\square$ and $108\,\Omega/\square$, correspondingly) [19,20]. The main stopping factors are careful control of diameter and chirality during synthesis or proper post-synthesis control of final characteristics. However, the R_{90} performance of pristine SWCNTs, achieved after the aerosol synthesis remained at a relatively low level of $250 \div 500\,\Omega/\square$ (recently the value of $65\,\Omega/\square$ was achieved for highly individual nanotubes by Mustonen *et al.*) [21]. Also, the nanotubes requiring surfactant or liquid cleaning, reach only insignificant values of $110\,\Omega/\square$ at $T_{550} \approx 80\%$. Other deposition schemes have also been proposed, but so far the post-treatment is assumed to be the most efficient way to solve the ITO replacement task (Figure 2.3-1).

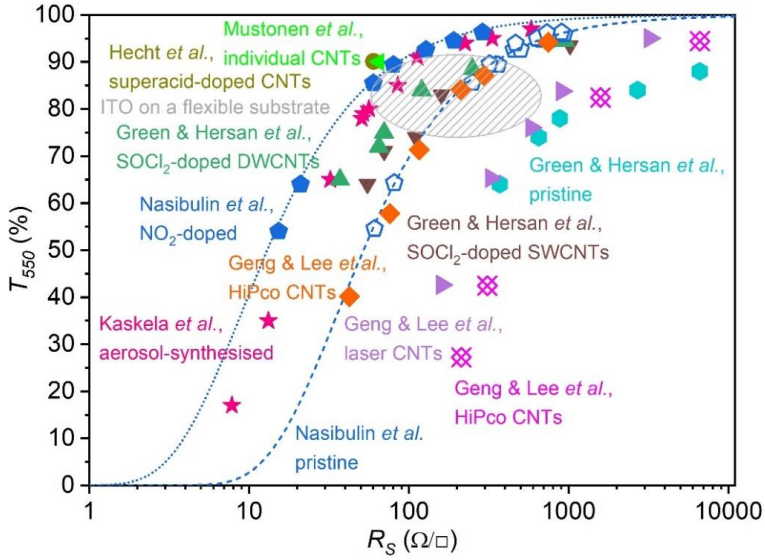

Figure 2.3-1. The reported optoelectronic performance of SWCNT-based TCFs and the best commercial flexible ITO-based electrodes. Dependence of the optical transmittance at 550 nm (T_{550}) on the sheet resistance (R_S).

2.3.1 Aerosol CVD synthesis

Among the various synthesis approaches, aerosol CVD (floating catalyst) is proved to be a unique and reliable technique to produce high-quality SWCNTs with tunable parameters. The main advantages of this method are high purity and uniformity of the product, a high-yield process completely free from liquid phase or surfactant cleaning, reduced bundle formation and flexibility in terms of substrate selection. All the mentioned results in outstanding optoelectronic and mechanical properties of nanotube films [8].

Because of plenty proven advantages, the aerosol CVD SWCNT synthesis technique was used for this work. Briefly, the synthesis is based on catalyst thermal decomposition and carbon monoxide (CO) disproportionation reaction on a catalyst particle surface. During this process, catalyst particle formation and subsequent growth of SWCNTs take place directly in the reactor flow (Figure 2.3.1-1). The reactor consists of a quartz tube placed in a furnace (hot zone), a precursor cartridge (filled with ferrocene/SiO_2 mixture) and a gas supply system (Figure 2.3.1-1). Catalyst precursor (ferrocene) vapor is delivered into the reactor hot zone by passing a gas stream (CO) through the pre-heated up to 60 $°C$ cartridge. Additionally, the flow of CO and carbon dioxide (CO_2) mixture passes through the reactor. Here, CO_2 increases the catalyst lifetime as it preserves the catalyst from deactivation [22,23]. The addition of CO_2 helps to control the output parameters of produced SWCNTs (for instance, longer nanotubes can be yielded at long catalyst lifetimes) as well as other synthesis

conditions. The typical synthesis temperature range is from 750 to 1100 °C. Therefore, after partial ferrocene decomposition and catalyst particle formation in the hot zone, the catalytic CO disproportionation takes place along with the decomposition of hydrocarbon and ferrocene, which eventually lead to the dissolution of carbon into nanoparticle (NP). As a result, this ends up with NP saturation by carbon and carbon layer formation on the catalyst particle surface (SWCNT are formed in case when catalyst particle size is less or equal to 5 nm, core shells – when the size is larger than that).

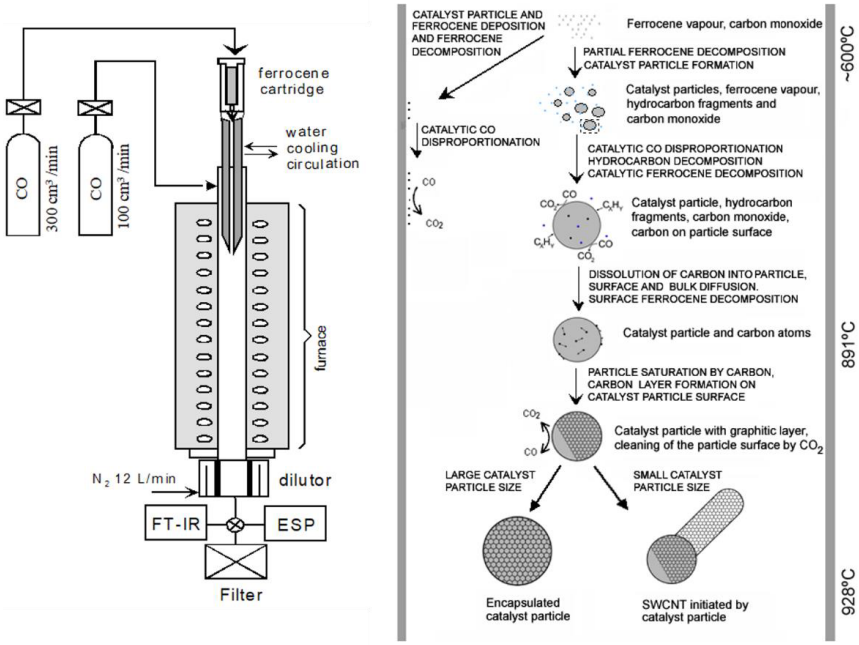

Figure 2.3.1-1. Typical SWCNT aerosol-synthesis reactor (left) and SWCNT formation scheme during the synthesis process (right) [7,8,23].

2.3.2 Optical properties

SWCNTs have a rather unique structure (similar to a graphene cellular lattice) that gives rise to their quasi-1D electronic structure with a specific optical absorption spectrum. Compared to ordinary bulk solids (3D materials), the absorption spectrum of SWCNT films shows sharp or broad peaks corresponding to transitions between van Hove singularities (vHs). Those characteristic peaks appear as a result of dipole-allowed transitions between the i-th conduction and valence band of vHs and are marked as E_{ii}^{j}, where j index stands for metallic (M) or semiconducting (S) nanotubes (Figure 2.3.2-1). Other transitions between the i-th and j-th band are not optically active. Thus, the optical response of nanotubes is related to the bandgaps of semiconducting and metallic nanotubes. Also, due to the quasi-1D nature of SWCNTs, exciton effects

play an important role in their electrodynamics, which results in the broadening of the absorption lines. Typically observed peaks in the UV-Vis-NIR region of optical absorbance are shown in Figure 2.3.2-1. The spectrum in a broad wavelength range (not limited to UV-Vis-NIR region but also including THz) can provide various additional information (average nanotube length, defects, *etc.*), despite the simple Beer-Lambert law in a visible region that is usually used to determine the film thickness. Generally, to characterize TCFs the absorbance or transmittance at a visible wavelength range of $400 \div 700\ nm$ is sufficient, while the value at $550\ nm$ is most frequently used for calculations due to the maximum spectral sensitivity of the human eye in daylight conditions.

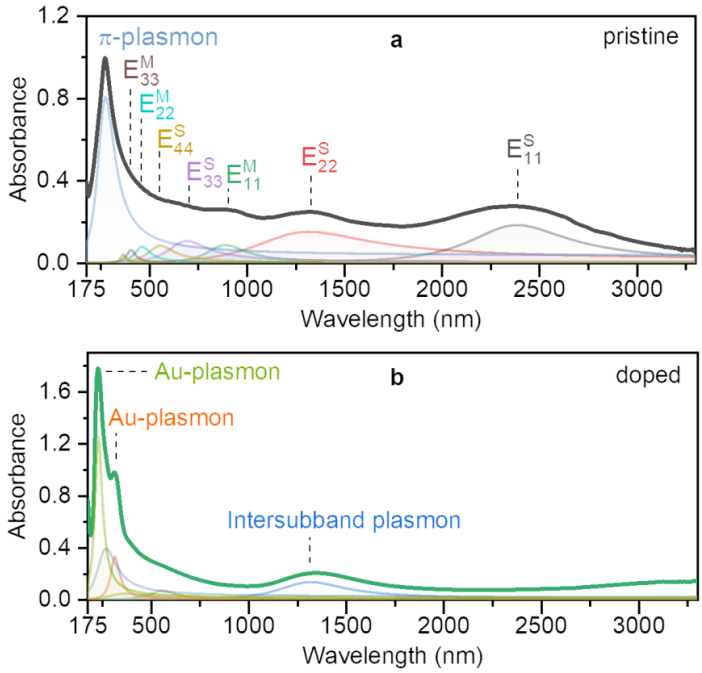

Figure 2.3.2-1. Typical absorbance spectrum and the fitted peaks (after baseline subtraction) of the (a) pristine and (b) doped SWCNT films. The films are large-scale and obtained by aerosol-synthesis technique.

2.3.3 Electronic properties

Aerosol-synthesized SWCNT films used for this study consist of a fraction of 1/3 metallic or 2/3 semiconducting nanotubes; therefore they have a certain bandgap and chirality values, transfer and absorption properties. The statistical fractioning of randomly oriented SWCNTs in films limits the conductivity by the introduction of Schottky barriers onto the nanotube contacts, which leads to contact resistance that cannot be overcome without further modification process. As can be seen, both the electronic and optical data analyses are

required to understand the structure of energy zones of the chirality distribution.

Due to the strong electron confinement in CNTs, the starting point of studying quantum properties is an understanding of available electronic states and possible excitations. Usually, to acquire an accurate energy band picture, the traditional zone-folding approach is used. Based on the tight-binding (TB) model for graphene, it was later replaced with the so-called extended tight-binding (ETB) model. The ETB model is based on the calculation of excitonic wave functions by solving the Bethe-Salpeter equation within the TB model. The screening effect of the π-electrons in CNTs is included. The unscreened Coulomb potential between carbon π-orbitals is modelled by the Ohno potential [24,25], which realistically describes organic polymer systems. Then further corrections due to the many-body (MB) effects with excitons and electron-electron interactions, were taken into account. Thus, there is a significant difference between the simple TB approach, which is widely used by researchers for its simplicity, and the ETB-MB model, which gives the closest results to the experimental data.

Based on the quantum nature of SWCNTs, their electronic structure can be described with TB models which consist of series of vHs resulting from 1D quantum confinement in nanotubes. The unique property of vHs is that the peak positions are determined by the diameter and chirality of the SWCNTs [26]. The energy difference between the vHs is inversely proportional to the diameter of the nanotubes ($E_{ii}^{j} \sim 1/d$). Therefore, as the nanotube diameter increases the singularities become closer to each other. In the case of SWCNTs with a very large diameter, the vHs are merged and the density of states (DOS) approaches the DOS of graphene. On the contrary, nanotubes of small diameters exhibit distinct 1D spikes. As a result, the transition in optical spectra occurs due to the transitions between vHs from the valence band to the conduction band through light absorption (related to the change in absorbance as in Figure 2.3.2-1). In the case of semiconducting nanotubes, E_{ii}^{S} transitions are allowed due to the selection rules, while in the case of metallic nanotubes only E_{ii}^{M} transition occurs with larger energy gap between vHs.

2.3.4 Doping

The fact that SWCNT films revealed various outstanding optical and electronic properties but still have an issue with the reduction of Schottky barrier between semiconducting and metallic nanotubes has led to several processing methods to increase their optoelectronic characteristics. The techniques are based on the shift of the Fermi level (E_F or E_F^j, where j stands for metallic (M) or semiconducting (S) nanotubes) position. VHs of SWCNTs discussed in the

previous section determine the E_F position. In pristine nanotubes the E_F is usually located in the middle of DOS. Therefore, if the electrons or holes are added to SWCNTs, the E_F is shifted upward (*n*-type doping) or downward (*p*-type doping), compared to the initial position (Figure 2.3.4-1), and conductivity increases. Normally, due to the presence of oxygen and moisture in the atmosphere, nanotubes become *p*-type doped, which is again related to the shift of E_F under ambient conditions.

According to the hybridization theory, SWCNTs (discretized system with energy levels) consist of two types of hybridizations – sp^2 and a small degree of sp^3 due to the curvature. Hence, the electronic properties correspondingly depend on the chiral indexes of nanotubes, which determine their metallic or semiconducting nature.

Among several key strategies to modify the charge carrier type (substitutional doping, doping in an electrostatic field, work function change ($\Delta\Phi$) when connected to the metal, ambipolarity, *etc.*), the adsorption doping has numerous advantages [27–29] and is selected as the core method in this thesis. The feasibility reason for this method is the exposure of all carbon atoms of SWCNTs to the environment. In this way, any atom/molecule put on a SWCNT causes charge transfer between the atom/molecule and a nanotube. Thus, the selection of an appropriate chemical dopant that will be put on the SWCNTs is highly important to achieve the desired conductivity. Additionally, adsorption doping does not affect and add many defects to SWCNT film, it is inexpensive and easy to scale if compared for instance with ordinary substitutional doping used in the semiconductor industry.

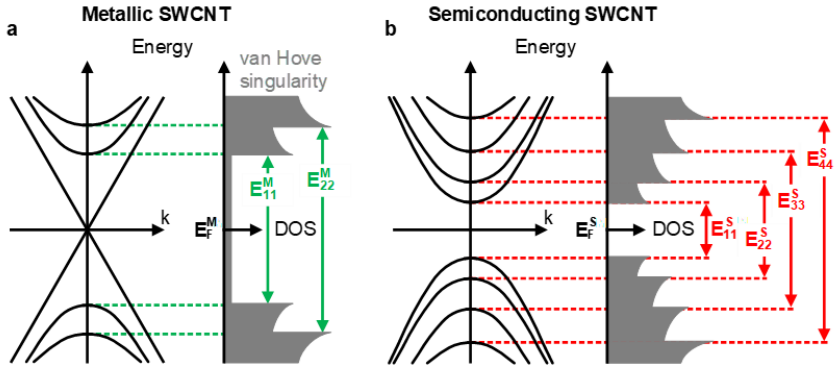

Figure 2.3.4-1. Illustration of the electronic band structures and density of states (DOS) of (a) metallic and (b) semiconducting SWCNTs.

There are two main effects in the literature that govern doping [30–35]: electronegativity (in case of doping with atoms) and electrochemical potential (when doping with molecules). Both of them lead to the two main results of doping: a shift of E_F and an increase in the electron (*n*-doping) or hole (*p*-

doping) carrier concentration. Additionally, the dopant may intercalate between SWCNT bundles and decrease the contact resistance between semiconducting and metallic nanotubes (reduction of the Schottky barrier height). Also, it is very important to estimate the position of E_F for a mixture of nanotubes in a film that has different DOS and consequently vHs. Therefore, simply by knowing the electronegativity or electrochemical potential (E_{NHE}^{j}, where j stands for the SWCNT or dopant and NHE – for normal hydrogen electrode used to experimentally determine the potential) *vs*. distribution relations for nanotubes and the selected dopant, the doping process can be done with the depletion of energetic states related to the vHs, which in turn will lead to the disappearance of related peak in the absorbance spectrum and change in the work function (Figure 2.3.4-1 and Figure 2.3.4-2). To relate the work function (Φ) and electrochemical potential, the work function of SWCNTs is converted to the electrochemical potential value with the two equations: $E_{NHE}^{dopant} = \Phi/e - 4.44$ (describes the reduction potential of a molecular dopant, where E_{NHE}^{dopant} is the electrode potential of the dopant to the NHE and $4.44\,V$ stands for absolute potential of the NHE in an aqueous solution at $295.05\,K$) and $E_{NHE}^{SWCNT} = a/d_t + b$ (describes the redox potential of the corresponding vHs of SWCNTs, where a and b are the fitting parameters and d_t is the diameter of a nanotube). For the esperimental estimation of the redox potentials of SWCNTs, electrochemistry with photoluminescence and optical absorption spectroscopy are utilized [36,37]. Figure 2.3.4-2 illustrate the dependence of an electrochemical potential of SWCNTs on the chirality/diameters, where c_i and v_i are the corresponding conduction and valence bands of metallic (solid green) and semiconducting (solid red) nanotubes, E_F^j denotes the Fermi level of metallic "M" and semiconducting "S" nanotubes. By using these plots, the adsorption dopants are selected to engineer the work function of SWCNTs. Additionally, while there are quite many stable *n*-type dopants [38,39] (not shown in Figure 2.3.4-2), the issue is to find a comparable *p*-type one.

As previously discussed, the doping ability of various *p*-type dopants is closely related to the reduction potentials of the chemicals (their electrochemical potentials) they consist of. If the electrochemical potentials of SWCNTs are compared against the reduction potentials of various chemical dopants:

$$\mathrm{DDQ}\ (0.51\,V) \ < \ \mathrm{NOBF_4}\ (1.34\,V) \ < \ \mathrm{AuCl_3}\ (1.49\,V),$$

it is clear that $AuCl_3$ has the highest positive reduction potential that makes it the strongest *p*-type dopant for SWCNTs (Figure 2.3.4-2). This is in good agreement with experimental observations.

Despite the fact that $AuCl_3$ is shown as the strongest *p*-dopant, it has some drawbacks, including hygroscopic effect, decrease in T_{550}, environmental

stability, and high cost. Therefore, research to estimate the potential for further E_F reduction or increasing the current work function values in p-type doped SWNCT films is to be continued in order to obtain highly transparent as well as conductive SWCNT-based films.

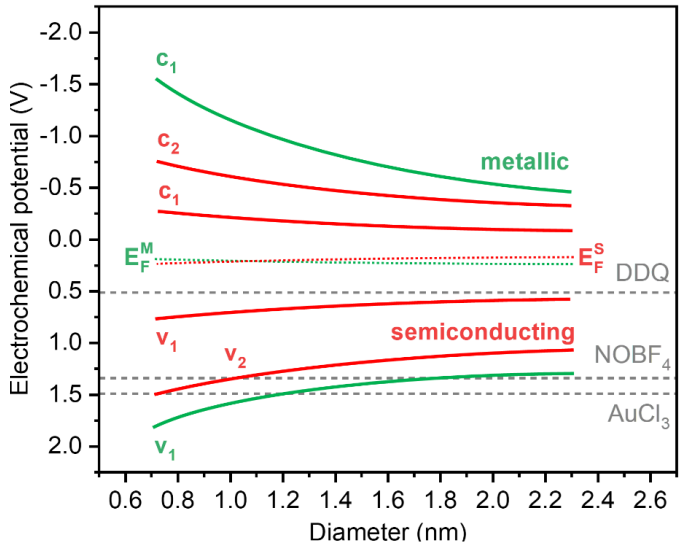

Figure 2.3.4-2. Illustration of the electrochemical potential dependence of corresponding conduction c_i and valence v_i bands of metallic (solid green) and semiconducting (solid red) nanotubes as well as related to them Fermi levels E_F^j (dotted green j = "M" and red j = "S", correspondingly), and p-type dopants (dashed grey) on a SWCNT diameter [40].

3. Methods

Basics of optical, electrical and aerosol measurement methods and techniques including the main parameters of the equipment used throughout the thesis are given here.

3.1 Optical measurements

As the electronic structure of SWCNT films depends on the nanotube chirality distribution, probing the material with the electromagnetic radiation of a particular wavelength/energy can reveal properties of individual nanotubes as well as the whole network of connected nanotubes. Thus, film morphology, nanotube alignment, diameter, length, and chirality distribution, metallic and/or semiconducting nature, conductivity, Fermi level, and work function values can be understood and calculated.

In general, the broad wavelength spectrum (spectrum consisting of ultraviolet (UV), visible (Vis), near-infrared (NIR), infrared (IR), and terahertz (THz) regions) can be measured and analyzed to explain some characteristics of SWCNT films. Usually, the peak nature analysis is only done after the fitting of the measured spectrum and can be divided into several critical spectral regions (Figure 3.1-1).

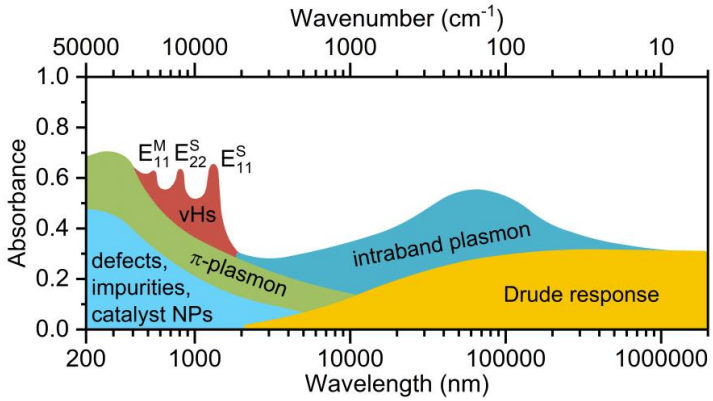

Figure 3.1-1. Illustration of the typical absorbance spectrum of a pristine randomly oriented SWCNT film at room temperature revealing the main peak contributions at different wavelength regions.

In addition to the information extracted from the broad wavelength regions, resonant Raman spectroscopy, X-ray photoelectron spectroscopy (XPS), ultraviolet photoemission spectroscopy (UPS), and optical microscopy serve as independent optical analysis techniques that can confirm the optical absorption spectroscopy (OAS) data.

3.1.1 UV-Vis-NIR spectroscopy

UV-Vis-NIR OAS is a common and robust technique to study SWCNTs, especially for TCF applications that depend on the transmittance value T_{550}. In addition to that, the film thickness can be easily estimated when the absorbance is known. The typical set-up consists of a white light source, diffraction mirrors enabling wavelength selection and detectors, covering the studied wavelength range.

The quantum nature of electronic states of a nanotube reflects in its optical spectra: diameter and chirality dependent peaks corresponding to the vHs are observed and could be utilized for quantitative characterization of chirality fraction. The position of peaks described is the same as for Raman spectroscopy (Section 3.1.3) and photoluminescence (resonant excitation wavelength) and determines the electronic structure of SWCNTs. These peak positions can be calculated using TBM taking into account excitonic effects [3] as discussed in Section 2.3.3.

The main issue to properly attribute the observed peaks related to the UV-Vis-NIR technique is the subtraction of background, mainly corresponding to the contribution of π-plasmon (Figure 3.1-1) – the collective oscillation of conductive band electrons in transverse to nanotube axis direction [41]. Also, light scattering on defects, impurities, and catalyst NPs have an impact on the background (Figure 3.1-1). Therefore, for careful analysis of the interband transitions (vHs related peaks), the background should be reasonably described mathematically. In the work of Pfohl *et al.* [42], a review of current approaches to this task was presented. The combination of Fano and Lorenztian line-shapes turned out to be the best to describe the background of SWCNT spectra in this region.

When the background is subtracted, obtained spectra must be fitted as a combination of many peaks corresponding to different chiralities. As a peak line-shape, the Lorentzian line is the most common choice [43], however, Voigt function (a combination of Gaussian and Lorentzian profiles) is more preferable in terms of accuracy [44].

In this thesis, UV-Vis-NIR OAS measurements were conducted on the aerosol-synthesized SWCNT films that were dry-transferred [7] onto optically transparent quartz or thermoplastic polymer (polyethylene terephthalate (PET)) substrates or prepared in the free-standing form (with no supporting

substrate). The transmittance ($T = I_{sample}/I_{reference}$, where I_{sample} and $I_{reference}$ are the light intensities passed through the sample and reference beam paths) or absorbance spectra were acquired using a dual-beam path UV-Vis-NIR spectrometer (Perkin-Elmer Lambda 1050) with a clean reference sample (quartz or PET) in the reference beam path or with no of such in case of the free-standing sample. The instrument allowed measurements over a wide wavelength (wavenumber) range from 175 ($\sim$57,000 cm^{-1}) to 3,300 nm ($\sim$3,030 cm^{-1}).

For the estimation of the main optical transitions, present in the UV-Vis-NIR spectra of the pristine/doped films, the experimentally measured data were fitted with a complex model, which is a linear combination of Lorentzian contours and exponential decay (Figure 2.3.2-1). Following the models, widely discussed elsewhere [44], the absorbance background was fitted with an exponential law $A_{background} = B \cdot e^{-b \cdot \lambda}$, which is the part of absorbance due to the presence of catalyst particles, amorphous carbon, *etc.* In the exponential law, B and b are the fitting parameters, where B accounts for the film density and thickness, while b depends on the amplitude and width of the plasmon coming from amorphous carbon and catalyst particles as discussed previously. The intense peak at 275 nm comes from π-plasmon, which was fitted with Lorentzian [45]. Remaining peaks correspond to E_{ii}^{S} and E_{ii}^{M} excitations and are usually fitted with Lorentzian, Gaussian or Voigt contours [42]. Here, Lorentzians were used following the model discussed elsewhere [43]. Fitting of spectral data after the doping provides the explanation of OAS peak behavior related to optically allowed transitions seen in the DOS, and thus the change in the work function and E_F^j shift (compare Figure 2.3.2-1a and Figure 2.3.2-1b).

In pristine nanotubes, we can clearly observe semiconducting E_{ii}^{S} transitions up to 55 and metallic E_{ii}^{M} up to 33, whereas in highly doped samples only high energy transitions survive, and new peaks at 1318, 315, and 230 nm appear (Figure 2.3.2-1b). The peak at 1318 nm was recently discussed [46,47] and its origin was attributed to the intersubband plasmon. The new peaks for the doped sample at 315 and 230 nm are supposed to come from gold NPs.

3.1.2 IR-THz spectroscopy

The advantage of the IR-THz spectral region is that contrary to the UV-Vis-NIR one it does not give the intrinsic information about individual nanotubes in the large-scale SWCNT films but provides their macroscopic parameters instead. Hence, IR-THz spectroscopy is useful for electrodynamic characterization of the charge carriers (bound and unbound) in pristine and doped films, understanding of the interaction of alternating current (AC) fields with the charge carriers as well as for determination of the distribution of nanotube

lengths in the films. As a result, complex permeability, direct current (DC) conductivity (in the limit of low THz frequencies), collision time, scattering rate, mean-free path, mobility, charge density, conductivity pathways, and other characteristic length are estimated within the Drude conductivity model describing this spectral region. All the mentioned also means that for the randomly oriented films with the Schottky barrier heights induced by inter nanotube contacts, the obtained characteristic values should be less than those quantities for the individual SWCNTs.

In this thesis, the SWCNT films of different thicknesses were prepared for IR-THz spectroscopy in the freestanding form to illuminate the influence of the substrate on the resulting spectra. The electrodynamic response of the freestanding films was measured in the range of wavelength (wavenumbers) from $625\,nm$ ($\sim 16{,}000\,cm^{-1}$) up to $2{,}000{,}000\,nm$ ($\sim 5\,cm^{-1}$) using three different spectrometers as described below. In addition to ordinary spectral analysis, one film with $T_{550} = 65\%$ was selected to study the broad wavelength spectra in a wide temperature interval (from $300\,K$ down to $5\,K$) to reveal and confirm the peak nature. All films were studied in the transmission geometry ($T = \left|T_{coefficient}\right|^2$, where $T_{coefficient} = \left|T_{coefficient}\right| \cdot exp(i\varphi)$ and φ is the transmission coefficient and phase shift, correspondingly). As a consequence of the joint analysis of THz and IR data, the spectra of broad-band conductivity and permittivity of the samples were obtained.

The THz-sub-THz spectra of the films were measured by continuous-wave (CW) spectrometer based on backward-wave oscillators (BWOs) and by the commercially available pulsed time-domain (TD) spectrometer TeraView. Both of these terahertz spectrometers operate in a quasi-optical regime (with no waveguides) and allow the direct determination of the spectra of real σ_{real} and imaginary $\sigma_{imaginary}$ parts of the optical conductivity, without the use of Kramers-Kronig analysis that is a regular procedure in the Fourier-transform-IR (FT-IR) spectroscopy where just one quantity is determined experimentally – reflection or transmission coefficient. The BWO-spectrometer operates in two modes [28]. In the transmission amplitude mode, the frequency-tunable monochromatic radiation passes through an empty aperture that is covered afterwards by a plane sample under study; the division of the two recorded spectra provides with the $T_{coefficient}$ of the sample. The transmission phase mode utilizes the Mach-Zehnder interferometric scheme. During frequency scanning, the position of the movable mirror in the reference channel of the interferometer is recorded at each frequency, which provides a minimum of the interference. This is done when there is no sample in the measurement channel and with the sample placed in it; the difference between the two data arrays provides with the spectra of the phase shift φ of the radiation passed through

the sample. Two measured quantities, $T_{coefficient}$ and φ, allow to determine the two required optical parameters, σ_{real} and $\sigma_{imaginary}$, using standard Fresnel equations for a layer. In TD spectrometers, the sample is subjected to a ps pulse that contains frequency components from about 0.3 THz up to $several\ THz$. The position and the amplitude of the pulse are detected when the measurement channel is empty or "blocked" with the sample. The difference in time between the two peaks is a measure of the radiation delay caused by the sample, and the amplitudes of the peaks give the measure of radiation absorption in the sample. Going from a time domain to a frequency domain is realized with the FT, and results again in the spectra of transmission coefficient of amplitude $T_{coefficient}$ and phase φ and a subsequent determination of the σ_{real} and $\sigma_{imaginary}$ spectra of the sample under study. Above THz frequencies, in the IR range, spectra of amplitude of the $T_{coefficient}$ is measured with a standard FT-IR spectrometer (Bruker Vertex 80v). The sample is placed in one of the arms of Michelson interferometer with a movable mirror. The intensity signal called an interferogram that is a superposition of all the monochromatic components of the light source is recorded by the IR detector as a function of the path difference of two beams of the interferometer. After taking FT of the interferogram (conversion of the space domain into the wavelength domain), the resulting spectrum is obtained. In order to exclude the spectrum of source and instrument functions of all-optical elements of the spectrometer from the resulting transmittance spectrum, the measured spectrum of the sample is divided into a spectrum measured without the sample.

3.1.3 Raman spectroscopy

One of the benefits of Raman spectroscopy (or resonant inelastic Raman spectroscopy) in SWCNT studies is that it can non-destructively provide numerous information about nanotubes in the film (defect and doping level, chirality and diameter distribution, *etc.*). However, in this case, at least several laser sources are required to be incorporated into a single set-up. Otherwise, only SWCNTs that are in the resonance with a particular laser are characterized.

Raman spectroscopy utilized here refers to the detection of the most standard Raman scattering component (Stokes component). Physically this means that the energy of a scattered photon ($\hbar\nu - \hbar\omega$) is lower than that of an incident one ($\hbar\nu$) due to generation of a phonon ($\hbar\omega$). Thus, a laser source of the Raman microscope is used to excite vibrational oscillations of sample molecules resulting in non-elastic scattering of the light: the energy of scattered photons is slightly smaller than incident ones. The energy difference is equal to vibration state energy. After that, the signal is filtered by a low pass filter to remove the incident and elastically scattered light and enters the spectrometer.

The main features of the Raman spectrum of any material are related to its phononic structure and represent features of lattice and defects. In the case of SWCNTs, there are four main features of Raman spectra: radial breathing modes (RBMs, $100 \div 500\ cm^{-1}$), D mode ($\sim 1350\ cm^{-1}$), G mode ($\sim 1590\ cm^{-1}$), and 2D mode ($\sim 2650\ cm^{-1}$) [48].

The vibrations corresponding to RBM peaks represent the radial contraction of a whole nanotube (analogy with breathing process). The energy of oscillations is reverse proportional to the nanotube diameter. That is why RBM is one of the main features of SWCNTs, which is used to determine SWCNT diameters $d[nm] = 248/\omega[cm^{-1}]$ [49]. Taking into account the resonance nature of Raman response (strong dependence on the excitation wavelength), even the particular nanotube chirality assignment is possible [50]. This assignment requires the use of the Kataura plot that relates the bandgap energies (*e.g.* E_{ii}^{S} and E_{ii}^{M} described in Section 3.1.1) of SWCNTs with their diameters.

G band is a result of excitation of Γ-point (center of the Brillouin zone) photon, which corresponds to out of phase oscillations of carbon atoms when all of them move along the same axis. Such kind of vibrations can be either in a direction parallel to nanotube's axis or in a perpendicular one. Due to the curvature of a nanotube (and thus its chemical bonds), G band splits into several components called G^- and G^+, which are excited in single-resonant scattering processes [51].

Both D and 2D peaks in Raman spectra of SWCNTs are the results of a double-resonant scattering process involving phonon and defect/impurity (D-mode) or 2 phonons (2D mode). A high ratio of 2D and D intensities correspond to the high quality of CNTs [52].

In this work, Raman spectroscopy was carried out using a Thermo Scientific DXRxi Raman Imaging Microscope together with a diode-pumped solid-state laser operating at 532 *nm*. The output laser power was set to 0.1 mW (power not destroying and heating both pristine and doped samples). The laser spot was focused with long working distance $50x$ objective and numerical aperture of 0.50. The signal accumulation time of 20 s and laser exposure time of 0.16 s were kept constant for all the samples. The measurement of the Raman signal intensity was repeated for at least 5 *times* at different positions. The SWCNTs were likewise transferred onto optical grade quartz substrates or measured in the free-standing form, yielding a negligible Raman background.

3.1.4 Optical microscopy

The morphology of pristine and doped SWCNT films was investigated by Leica DM4500P optical microscope in a non-polarized transmitted light mode with dark- and bright-field illumination set-ups. This simple and fast technique allows seeing the film surface with its μm-sized defects (dark-field illumination)

as well as overall film transmittance (bright-field illumination). For a pristine film that is a porous structure, it leads to a scattering effect of the incident light on a randomly-oriented network of nanotubes. The effect is pronounced for the thick films of $T_{550} \leq 80\%$ and depends on the observation angle. Contrary, when the thick film is doped or densified (film thickness d decreases), the effect of scattering vanishes and that leads to the increase of transmittance. An interesting observation happens when the same doping or densification procedure is applied to thin films of $T_{550} \geq 90\%$ with almost no scattering seen. The film thickness d again decreases while the transmittance decreases also. For thin films, this transmittance decrease is attributed to the increase in film refractive index n, on the assumption of constant $d \cdot n$.

3.1.5 XPS and UPS

X-ray photoelectron spectroscopy (XPS) or as it is also called electron spectroscopy for chemical analysis, allows studying physical and chemical phenomena happening on the surfaces of pristine or doped SWCNT films. This technique utilizes X-rays to measure the binding energy (BE) of the electrons in the orbitals of the atoms. Ultraviolet photoelectron spectroscopy (UPS) serves as one of the best ways to determine and confirm the absolute work function of the SWCNTs. UPS measurement results combined with XPS analysis give an understanding of the intrinsic work function values of pristine nanotubes as well as dopant influence on the SWCNT electronic structure after the doping. Additionally, OAS with the vHs transitions can be used as a work function confirmation technique. Here should be noted that OAS gives only the range where the work function is, while UPS gives it precisely. Also, as the sources used for XPS and UPS are different, the penetration depth and resolution are also. Ordinary the electrons are extracted only from the thin layer close to the surface and the penetration depth (resolution) is $\sim 10\ nm$ ($0.5\ eV$) and $\sim 2\ nm$ ($0.01\ eV$) for X-ray and UV sources, respectively. In addition to X-ray energy used to extract electrons is higher than that in UPS. This allows to extract core level electrons of the chemical compound probed, and these electrons are highly individual for the various compounds, that accept the clear determination of elements presented.

The samples in a freestanding form were prepared for characterization with XPS and UPS. The chemical composition and elemental analysis of pristine and doped samples were mainly carried out using Kratos Analytical AXIS ULTRA DLD XPS spectrometer fitted with a monochromatic Al Kα X-rays source and achromatic Mg Kα / Al Kα dual anode X-ray source in an ultrahigh vacuum chamber with the pressure of $\sim 10^{-10}\ mbar$. A monochromatic Al Kα anode ($1486.6\ eV$) was selected and operated at $150\ W$ and $15\ kV$. XPS spectra were

recorded at 90° takeoff angle from the surface of the sample holder using an aperture slot of $300 \times 700\ \mu m^2$. UPS were also performed in the same UHV chamber using He (I) 21.22 eV photons. Samples were mounted on a stainless steel sample bar of $130 \times 15\ mm^2$. BE values were calculated on the basis of the C 1s peak at 284.6 eV. The relative atomic concentrations of detected elements were determined from the appropriate core level integrated peak areas and sensitivity factors provided by Kratos analysis software Vision 2.2.10 Shirley background subtraction was used for relative atomic concentrations calculation.

3.2 Electrical and electronic measurements

Since SWCNT films present promising material for flexible and stretchable electronic devices, sensors, microchips, screens, their electrical properties are widely exploited and many techniques are implemented to analyze their electrical transport and electronic characteristics for each particular application. This chapter gives a brief description of the most essential techniques to obtain high conductivity or low resistance values of SWCNT films after the doping, as well as to show nanotubes at a nm-scale level for metrological purposes.

3.2.1 Sheet resistance

For SWCNT-based TCFs resistance of thin films or sheet resistance (R_S) is the second crucial parameter after its transmittance value in the visible spectrum region (T_{550}). The lower the film resistance the better it suits electrode design.

Evaluation of R_S is usually done with four-point probe measuring set-ups. The resistance R is classically expressed by the material resistivity ρ, length L, and area S:

$$R = \frac{\rho \cdot L}{S} = \frac{\rho \cdot L}{W \cdot t} = \frac{\rho}{t} \cdot \frac{L}{W} = R_S \cdot \frac{L}{W},$$

where W and t are the width and thickness of the film. For the linear probe configuration, as in the system used throughout the thesis (Jandel RM3000), the sheet resistance is evaluated in the following way:

$$R_S = \frac{\rho}{t} = \frac{\pi}{\ln 2} \cdot \frac{V_{probe}}{I_{probe}}.$$

The idea of the linear probe configuration is to use four electrodes, which are linearly placed close to each other and far from the sample edges. Two electrodes are used to apply current (outer electrodes), while the other twos to register the voltage (inner electrodes). The separation of current and voltage electrodes eliminates the lead and contact resistance from the measurement. Since the measured resistance of the film depends on its thickness, usually two

more characteristics are calculated, which are convenient for comparison of different materials – the figure of merit (FoM) and equivalent sheet resistance (R_{90}) for a film with R_S and light absorbance at 550 nm (A_{550}):

$$FoM = \frac{1}{R_S \cdot A_{550}};\ R_{90} = \frac{R_S \cdot A_{550}}{\log(10/9)}.$$

Another approach for R_S measurements is the van der Pauw method, which was performed at Probe Station MPI TS 150. The idea is to apply a four-point probe placed around the perimeter of the sample, in contrast to the linear four-point probe: this allows the van der Pauw method to provide an average resistivity of the sample, whereas a linear array provides the resistivity in the sensing direction. To make a measurement, a current owing along one edge of the sample I_{12} and the voltage across the opposite edge V_{34} is measured. From these two values, the resistance is found using Ohm's law: $R_{12,34} = V_{34}/I_{12}$. Van der Pauw shows that the sheet resistance of a sample with arbitrary shape can be determined from two of these resistances – one measured along a vertical edge $R_{12,34}$ and a corresponding one measured along a horizontal edge $R_{23,41}$. The actual R_S is related to these resistances by the van der Pauw formula:

$$e^{-\pi \cdot R_{12,34}/R_S} + e^{-\pi \cdot R_{23,41}/R_S} = 1.$$

3.2.2 SEM and TEM

Electron microscopy techniques are powerful tools for the characterization of individual SWCNTs as well as the film morphology. For instance, a transmission electron microscope (TEM) provides resolutions of 1-5 Å and identification of elements in the single-atom scale [72]. Additionally, electron diffraction (ED) can be used to identify lattice structures, where the diffraction pattern is formed as a result of the interaction of electrons injected with the lattice atoms. As a consequence, ED is the only technique for correct identification of SWCNTs' chirality regardless of the nanotube parameters as diameter, dopant coating, *etc*. In this work, the morphology of pristine and doped SWCNT films was investigated by a scanning electron microscope (SEM) – FEI Helios 660 DualBeam SEM. FEI Tecnai G2 F20 TEM was used to analyze the structure and geometry of pristine SWCNTs. To minimize the destructive influence of electron irradiation all measurements were performed at the acceleration voltages of 3 kV (SEM) and 80 kV (TEM) and with minimal possible electron illumination time. For the TEM analysis SWCNTs were directly collected onto Lacey carbon-coated TEM grids. The collection time was optimized thus the measured optical transmittances (at 550 nm) of films were as required for the experiment.

3.3 Aerosol measurements

Differential mobility analysis (DMA) is a well-known technique in the field of aerosol science for the determination of particle number size distributions (NSDs) in the gas-phase. This measurement is based on the size classification of charged aerosol particles according to their electrical mobility, *i.e.* the ratio of their size to the charge they possess, in the electric field. The system is arranged so that particles with selected electrical mobility pass through the DMA and are carried to its outlet for number particle size concentration measurement with the condensation particle counter (CPC). Scanning the voltage between the DMA electrodes forming the electric field that enables determination of the particle NSDs within a particle size range regulated by the DMA flow rates, voltage range and geometry [21,53–55].

In publication II, the NSD of the particles left after the evaporation of droplets of pure solvent and dopant solution was measured by scanning mobility particle sizer spectrometer (Model 3938, TSI) as shown in Figure 3.3-1. The number particle size concentrations were measured by using CPC (Model 3788, TSI) combined with DMA (Model 3082, TSI). The measurement procedure was organized in the following way. The measured aerosol was transferred directly to the inlet impactor of DMA where the large droplets were taken away. Further, to have an equilibrium (Boltzmann) distribution of chargers the flow passed through the charger. Then, the mobility separation of particles was carried out in an electric field with the scanning operating voltage from 10 to 100 kV. The concentration of the mobility selected particles was measured in the CPC, where the particles first were grown to a detectable size and then counted.

Therefore, in principle and according to the discussed aerosol analysis, DMA measurements could help to reveal whether individual or bundled nanotubes are produced during aerosol CVD synthesis. Thus, a small total concentration of particles (basically less than $10^5\ \#/cm^3$) could be related to individual nanotubes (typical agglomeration time is less than the residence time), while a high effective diameter could be indirectly attributed to a long SWCNT length [21,54,56]. Both individuality and length are proved to be the keys parameters for transparent and conductive film development. Using DMA as an express tool of aerosol characterization, one can adjust synthesis conditions for the highest performance.

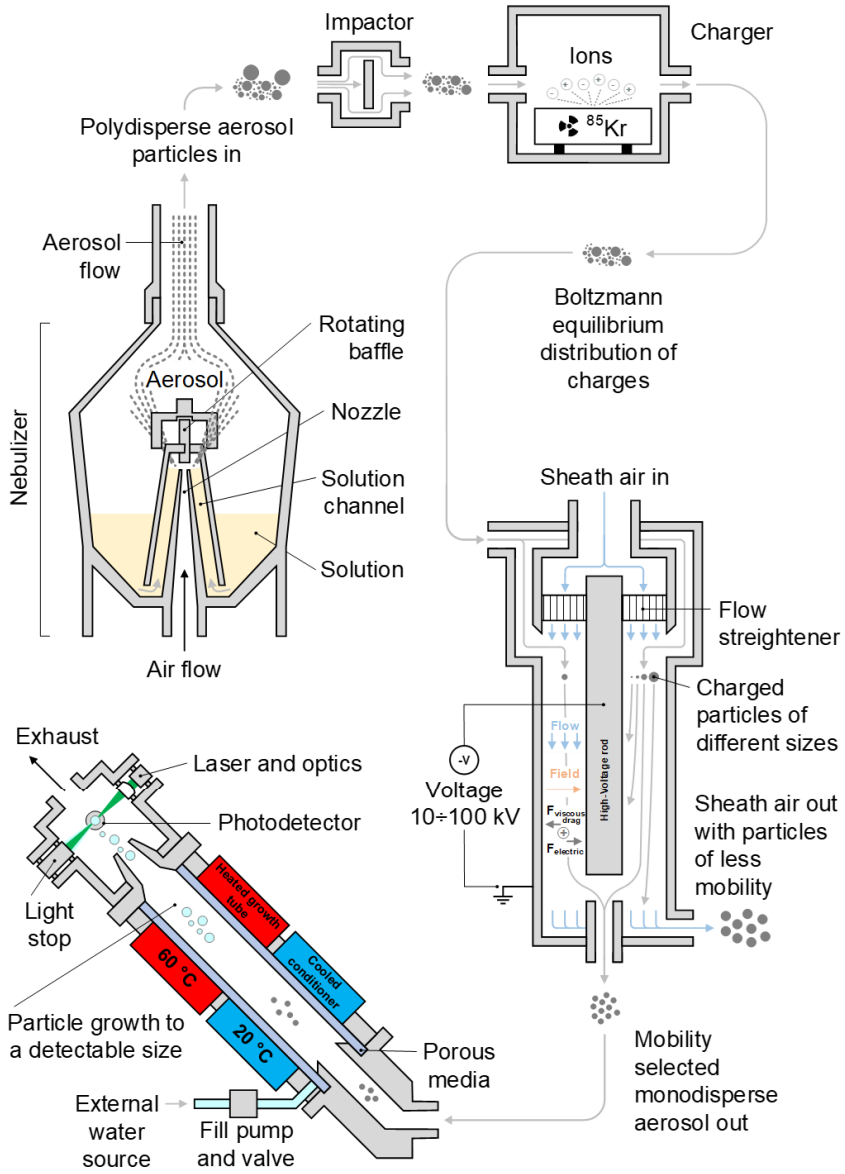

Figure 3.3-1. Illustration of the experimental setup used for size distribution measurements of the residual particles left after complete evaporation of droplets of pure solvent and dopant solution.

4. Results and discussion

Each of the section represents the main results obtained in Publications I-V.

4.1 Charge carrier dynamics

This chapter focuses on the broad wavelength spectrum features of both pristine and doped nanotubes. It explains how depending on the doping level, such characteristics as transmission ($T = \left|T_{coefficient}\right|^2$), conductance, and photoconductivity in THz-IR spectral regions can be effectively "tuned" to modify the optoelectronic properties of SWCNT films (Publications III-IV). The results introduced here enable fundamental understanding of processes occurring in the synthesized films and after doping, that provide researchers with key charge carrier parameters.

4.1.1 THz-IR electrodynamics

Due to the high porosity of pristine films their thickness cannot be precisely determined. Meanwhile, the results are discussed without assigning a certain thickness to all films and without specifying their internal structure. This approach allows comparing the effective optical properties of pristine and doped films. We use the model of complex conducting surface developed for conducting films whose thickness is less than the skin layer depth [57]. The complex conductance Y of such a layer is given by the Drude conductivity model:

$$Y = \sigma^*(\nu) \cdot d = \left(\sigma_{real} + i \cdot \sigma_{imaginary}\right) \cdot d = \left(\frac{\sigma_{\mathrm{DC}} \cdot \gamma^2}{\gamma^2 + \nu^2} + i \cdot \frac{\sigma_{\mathrm{DC}} \cdot \nu \cdot \gamma}{\gamma^2 + \nu^2}\right) \cdot d\,,$$

where $\sigma^*(\nu)$ is the frequency-dependent conductivity, d is SWCNT film thickness assuming that the film is homogeneous, σ_{real} and $\sigma_{\mathrm{imaginary}}$ are the real and imaginary parts of the conductivity, σ_{DC} is the DC conductivity and γ is the charge-carrier scattering rate.

Figure 4.1.1-1b,c,e,f presents $\sigma_{real} \cdot d$ and $\sigma_{imaginary} \cdot d$ conductance spectra of pristine and doped films ($T_{550} = 65\%$), which were measured at room temperature and 5 K.

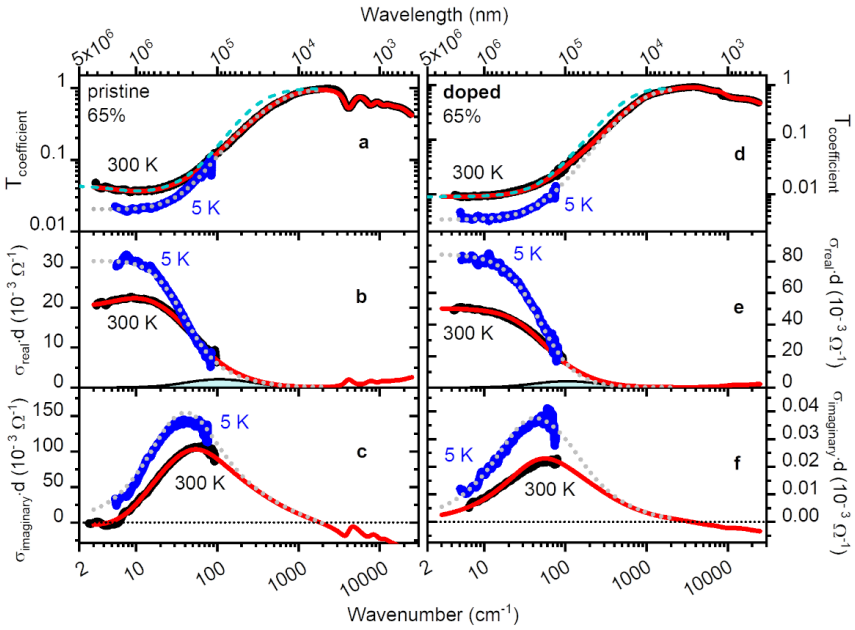

Figure 4.1.1-1. Room temperature 300 K (solid black lines) and 5 K (solid blue dots) spectra of (a, d) transmission coefficient $T_{coefficient}$, (b, e) effective real $\sigma_{real} \cdot d$ and (c, f) effective imaginary $\sigma_{imaginary} \cdot d$ parts of conductances of (a, b, c) pristine and (d, e, f) doped SWCNT films ($T_{550} = 65\%$). The fitting curves for 300 K and 5 K samples are shown in solid red and dotted grey, correspondingly. The THz-sub-THz region corresponds to direct measurements on the THz pulsed TD and CW backward-wave oscillator based spectrometers. Dashed cyan lines in (a) and (d) correspond to the fit when the absorption resonances at 100 cm^{-1} in $\sigma_{\mathrm{real}} \cdot d$ spectra (cyan-shaded areas in (b) and (e) show absorption peaks due to plasmon resonance) are not taken into account.

Above 3,000 cm^{-1}, pronounced minima connected with the interband transitions (vHs) are visible. A strong decrease in transmission below 1,000 cm^{-1} in the THz-IR region (Figure 4.1.1-1a,d) and the corresponding behavior of directly determined $\sigma_{\mathrm{real}} \cdot d$ and $\sigma_{\mathrm{imaginary}} \cdot d$ conductances (Figure 4.1.1-1b,c,e,f) are associated with the response of delocalized charge carriers since:

- the THz-spectra of $\sigma_{real} \cdot d$ and $\sigma_{\mathrm{imaginary}} \cdot d$ conductances have the form predicted by the Drude model of free-carrier conductivity: $\sigma_{real} \cdot d$ shows an increase towards low frequencies and $\sigma_{\mathrm{imaginary}} \cdot d$ displays distinct signs of a characteristic broad peak;
- low-frequency extrapolations of $\sigma_{real} \cdot d$ conductance are in reasonable agreement with the published DC values [58–60];

- the $\sigma_{real} \cdot d$ conductance shows a metal-like temperature dependence: $\sigma_{\text{real}} \cdot d$ increases when the SWCNT film is cooled down (Figure 4.1.1-1b,e).

We have obtained the broad-band THz-IR spectra of $\sigma_{real} \cdot d$ and $\sigma_{\text{imaginary}} \cdot d$ by selecting the merged THz and IR transmission spectra (Figure 4.1.1-1). The observed minima in transmission above $\sim 3{,}000\ cm^{-1}$ were modeled using regular Lorentzians. Lower-frequency spectra were modeled on the basis of the Drude expression for the complex conductance. It is important to stress that low-frequency (below $\sim 100\ cm^{-1}$) spectra of transmission were processed along with directly measured $\sigma_{\text{real}} \cdot d$ and $\sigma_{\text{imaginary}} \cdot d$ conductances that determine transmission at these frequencies. Such an approach allowed us to unambiguously define charge carrier parameters for the complex conductance expression (as described below).

We note that in order to consistently describe the transmission and conductance spectra we had to introduce an additional term in the form of an absorption band located at $\sim 100\ cm^{-1}$. It is indicated by the cyan-shaded areas in Figure 4.1.1-1b,e and was modeled by a Lorentzian. Another feature detected in the spectra of all pristine films was a decrease of $\sigma_{\text{real}} \cdot d$ in the direction of the lowest frequencies below $\sim 10\ cm^{-1}$ at $300\ K$ (Figure 4.1.1-1b).

To analyze the nature of the absorption band at $\sim 100\ cm^{-1}$, we plot its spectral shapes (insets in Figure 4.1.1-2a) for all pristine and doped films ($T_{550} = 65, 75, 80, 90,$ and 95%). It can be seen that the band intensity or spectral weight (area under the $\sigma_{\text{real}} \cdot d$ curves) is larger for the doped films and quickly decreases as the T_{550} value increases (inset in Figure 4.1.1-2b). This is a strong indication that the origin of the bands should be related to the presence of delocalized charge carriers. We associate these absorption peaks with plasmon oscillations of charge carriers which are partly localized by defects, impurities and nanotube intersections. Corresponding excitations have been previously observed in numerous experiments. The amplitude of the bands is much smaller than that of the free-carrier Drude component (characterized by the $\sigma_{real} \cdot d$ value at $\sim 10\ cm^{-1}$), which makes them not so clearly expressed in these experiments. We believe that the reason is the effective screening by both delocalized carriers and only a small fraction of localized carriers (compared to the number of delocalized carriers). The fact that the position of the bands is basically unchangeable in all studied films means that the localization distance of the carriers is determined not by the SWCNTs' ends [61], but by certain defects inside the nanotubes or their intersection. We can roughly estimate the distance between these defects as $L = V_p/(\pi \cdot \nu_p)$, where V_p is the plasmon velocity that is several times greater than the Fermi velocity [62] and ν_p is the plasma frequency. With $\nu_p = 100\ cm^{-1}$, $V_p = 4 \cdot V_F$ [62] and the Fermi velocity

$V_F = 10^8\ cm/s$ [62] we obtain $L = 0.4\ \mu m$. The Fermi velocity of $V_F = 10^8\ cm/s$ is a typical value for graphene-like materials, obtained using following equation: $(\sqrt{3} \cdot a \cdot \gamma_0)/(2 \cdot \hbar)$, where a – hexagonal lattice constant, γ_0 – nearest neighbor hoping integral, which is close to 3 eV for bulk graphite. With a mean-free path (l) in our films equal to $0.1\ \mu m$ (as discussed below), we have $l/L = 0.25$ confirming that our films are practically free of impurities [62]. The value $L = 0.4\ \mu m$ correlates well with the average distance between intersections of SWCNTs, as can be seen from the atomic force microscopy studies (Figure 2a-d in Publication IV). Thus, we assume that plasmon excitations occur due to reflections of the charge carrier plasma at the SWCNT intersections. Meanwhile, a more detailed study on this matter and THz-peak nature is required for complete understanding. Also, based on the fact that broad and strong THz conductivity peak appears in both types of nanotube films (semiconducting and metallic), whose behaviors are consistent with the plasmon resonance explanation, this firmly rules out other alternative explanations such as absorption due to the curvature-induced gaps [63,64].

To account for the low-frequency downturn of $\sigma_{real} \cdot d$ (which is proportional to absorption), observed in pristine films, we recall that their response is determined by two contributions to the DC/AC conductivity [60,65]. One of them is connected with the intrinsic conductivity of the individual nanotube or nanotube bundles. The other is governed by the fluctuation-assisted tunneling of charge carriers through the energy barriers at the inter nanotube contacts. Therefore, the total resistivity ρ_{DC} at a given temperature T is given by:

$$\rho_{DC}(\mathrm{T}) = \frac{1}{\sigma_{DC}(\mathrm{T})} = \rho_m \cdot exp\left(-\frac{\mathrm{T}_m}{\mathrm{T}}\right) + \rho_t \cdot exp\left(\frac{\mathrm{T}_t}{\mathrm{T}_s + \mathrm{T}}\right),$$

where T_m (parameter related with the phonon-related part of resistance), T_t (tunneling contribution) and T_s are the temperature-related parameters, the temperature $\mathrm{T}_m = (h \cdot v)/k_B$ accounts for the backscattering of the charge carriers within the individual SWCNT or nanotube bundle, the temperature T_t is related to thermal energy $k_B \cdot \mathrm{T}_t$ which corresponds to the typical energy barrier $E_t \sim k_B \cdot \mathrm{T}_t$ for carrier tunneling with k_B as the Boltzmann constant, the ratio $\mathrm{T}_t/\mathrm{T}_s$ determines the tunneling in the absence of fluctuations and thus the conductivity $\sigma_{DC}(\mathrm{T} \to 0)$ in the low-temperature limit, and ρ_m and ρ_t coefficients are temperature independent factors. The values of the tunnel gaps can be estimated as $1.4 \div 1.6\ meV$ (corresponding to temperatures $\mathrm{T}_t = 16 \div 18\ K$ [60]) for pristine SWCNT films and as $0.2 \div 0.25\ meV$ ($\mathrm{T}_t = 2 \div 3\ K$ [60]) for doped films (this estimation corresponds to the $CuCl_3$ doped films, but we expect that it does not differ much from the films doped with $AuCl_3$). Let $h\nu$ be the energy of electromagnetic radiation that probes the response of the film (h is the Planck's constant). Then, for this energy that exceeds much the tunnel gap

($h \cdot \nu >> k_B \cdot \mathrm{T}_t$) the radiation does not "feel" the presence of a small gap, and the charge carriers respond as if they were free. In another case, $h \cdot \nu < k_B \cdot \mathrm{T}_t$, the carriers experience an impeding tunnel gap leading to lower AC and DC conductivities. The same behavior is observed at $10\ cm^{-1}$ for pristine films, where the tunnel gap energy corresponds to a frequency of $11 \div 13\ cm^{-1}$. Similarly, in the spectra of doped SWCNT films measured at much higher frequencies, no signs of the tunnel gaps of $0.2 \div 0.25\ meV$ (corresponding frequencies are $1.4 \div 2\ cm^{-1}$) were found.

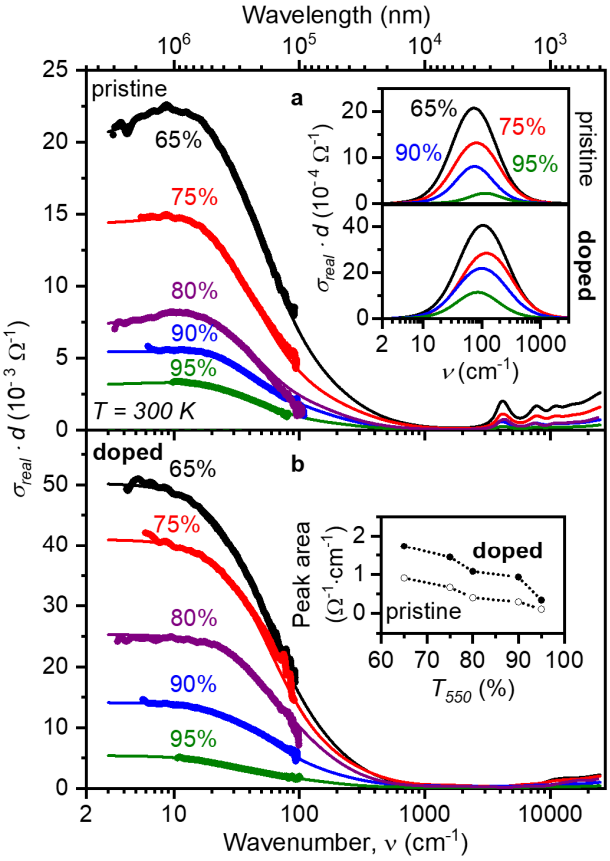

Figure 4.1.1-2. Room temperature spectra of the real part of conductance $\sigma_{real} \cdot d$ of (a) pristine and (b) doped SWCNT films (T_{550} = 65, 75, 80, 90, and 95%). Thick lines in the THz-sub-THz region correspond to direct measurements on the THz pulsed TD and CW backward-wave oscillator based spectrometers. Lines correspond to the least-square fit results, as described in the text. Insets show the (a) absorption peaks due to plasmon resonances in pristine and doped films and (b) dependences of the peak oscillator strengths (peak area under the spectra) for pristine and doped nanotubes on the T_{550} values.

Having identified the Drude-like component in the response of the films it is possible to extract effective parameters of corresponding charge carriers. A typical downturn towards high frequencies in real conductance $\sigma_{real} \cdot d$ or the peak position of the imaginary conductance $\sigma_{\text{imaginary}} \cdot d$ (Figures 4.1.1-1 and 4.1.1-2) provides the carriers' scattering rate γ which, in turn, allows to calculate: the effective mobility $\mu = e/(2 \cdot \pi \cdot m^* \cdot \gamma)$ – where e is the electron charge and $m^* = 0.2 \cdot m_e$ is its effective mass; the collision time $\tau = 1/(2 \cdot \pi \cdot \gamma)$; the mean-free path $l = \tau \cdot V_F$ (with the Fermi velocity of $V_F = 8 \cdot 10^7\ cm/s$) [66]. These quantities are plotted in Figure 4.1.1-3 where it is seen that they are practically independent of the film transmittances T_{550}. As expected, the obtained values of the mobility and mean-free path are much smaller than those of individual SWCNTs ($\mu = 1{,}000 \div 30{,}000\ cm^2/(V \cdot s)$ and $l = 1 \div 2\ \mu m$) [67,68] due to the effect of inter nanotube contact phenomena.

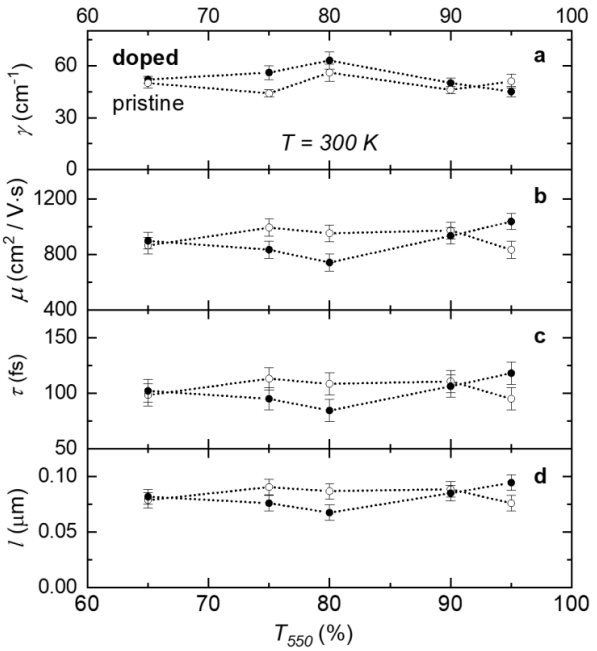

Figure 4.1.1-3. The effective parameters of charge carriers in pristine (empty circles) and doped (filled circles) SWCNT films as dependent on the film transmittance T_{550}: (a) charge carrier scattering rate, γ; (b) mobility, μ; (c) collision time, τ; (d) mean-free path, l.

Now we turn to the temperature dependences of the charge carriers' effective parameters which were determined for the film with $T_{550} = 65\%$ (Figure 4.1.1-4). The scattering rates for the pristine and doped films show similar behavior, with the values for the doped film being slightly larger. This can be due to the increased charge carrier concentration in the doped films and thus in the higher collision frequency and additional scattering on the impurities introduced by

doping, or due to the involvement of small wave vector phonons into the scattering processes in doped films, where the E_F is shifted down into the valence band. The overall temperature variation of charge carriers' parameters (scattering rate, mobility, scattering time, mean-free path) is similar to that observed in semiconductors for free carriers in conduction or valence band where they reveal metal-like frequency dependences of complex conductivity spectra (as in Figure 4.1.1-1). While cooling down the samples from the room temperature to $T \approx 100\,K$, the scattering weakens as phonon scattering gets frozen out; at lower temperatures – the impurity/defect scattering mechanism dominates.

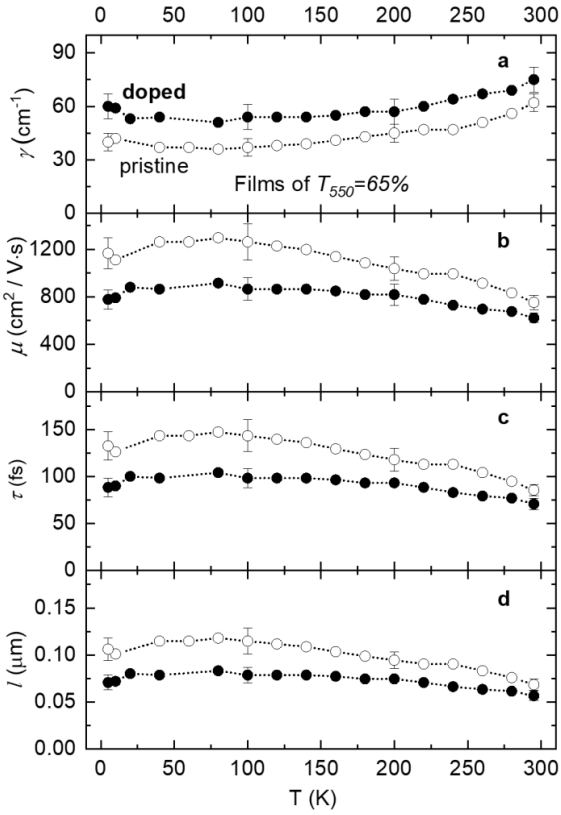

Figure 4.1.1-4. Temperature T dependences of the effective (a) charge carrier scattering rate γ, (b) mobility μ, (c) collision time τ, (d) mean-free path l of pristine and doped SWCNT films of $T_{550} = 65\%$.

Extrapolating the conductance of SWCNT films to the zeroth wavenumber (Figure 4.1.1-2), one can calculate that the sheet resistance of the $T_{550} = 90\%$ films lowered from 167 to 67 $\Omega/\square$ after doping. Such a low value of the sheet resistance for the SWCNT films indicates a high doping level, which leads to a significant shift of the E_F after doping, compared to pristine SWCNTs. This

results in an increase in the number of charge carriers and in a reduction of the Shottky barrier between SWCNTs and bundles.

Finally, we note that knowing the exact value of the film thickness would allow calculating the conductivity $\sigma_{DC} = n \cdot e \cdot \mu = n \cdot e \cdot (e/(2 \cdot \pi \cdot m^* \cdot \gamma)) = ((n \cdot e^2)/m^*) \cdot (1/(2 \cdot \pi \cdot \gamma)) = ((n \cdot e^2)/m^*) \cdot \tau = v_{plasma}^2/(2 \cdot \gamma)$ and, hence, the effective free charge carriers' concentration. Assuming the effective mass and film thickness for the pristine and doped films ($T_{550} = 90\%$) as $m^* = 0.2 \cdot m_e$ [69] and $d = 20\,nm$ [70], we obtained the concentration values of $1.9 \cdot 10^{19}\,cm^{-3}$ and $4.8 \cdot 10^{19}\,cm^{-3}$, respectively. Other values at room temperature for pristine and doped SWCNT films ($T_{550} = 90\%$), correspondingly, are: γ (63 and $72\,cm^{-1}$), μ (750 and $610\,cm^2/(V \cdot s)$), τ (90 and $70\,fs$), l (0.07 and $0.06\,\mu m$).

4.1.2 Negative THz photoconductivity

The THz-peaks nature of both pristine and doped material was further analyzed by means of an additional charge carrier analysis tool (pump-probe optical excitation) to examine the THz photoconductivity and its recovery dynamics in *p*-type doped nanotubes. These physical parameters and values of long SWCNTs produced by the aerosol-synthesis can be ideal for highly required TCF-based modulators, polarizers, emitters, saturable absorbers and detectors due to the modulation of the optoelectronic performance observed in Section 4.1.1 for the THz-IR spectral region.

Indeed, under the pump-probe optical excitation of 650 nm, both pristine and doped SWCNT films showed a giant (~60% more than the intrinsic nanotubes) photo-induced reduction of the THz conductance ($\sigma \cdot d$). The negative behavior of photoconductivity registered for SWCNT contrasts with the commonly observed enhancement in conductivity (positive photoconductivity) after the same optical absorption (for instance, for semi-insulating GaAs). The negative photoconductivity reported here is observed for all doping levels regardless of a gradual vHs change marked in the UV-Vis-NIR region with doping. A reduction of conductivity upon photoexcitation is linked with a decrease of Drude and plasmon spectral contributions (Figure 3.1-1 and 4.1.2-1), related to an increase in the scattering rate. The recession of the THz photoconductivity after excitation can be explained by the formation of excitons (which lower the concentration of free carriers) under photo-excitation and/or trions. The formation of these quasi-particles is explained from the Drude-Lorentz model (Section 4.1.1) since this theory explains the motion of charge carriers under the applied field $\sigma(\omega) = \frac{N \cdot e^2}{m^*} \cdot \frac{i}{\omega + i \cdot \gamma}$. Each of the charge carriers due to its own scattering affects the change in the scattering rate γ related to the change in carrier density $N \cdot e^2$ or effective mass m^*. Thus, the lower conductivity after

excitation in SWCNTs can be linked to the formation of excitons under photoexcitation (as the mass m^* changes), which rapidly form trions with a higher mass and lower mobility than unbound (free) charge carriers.

To analyze the change in spectral weight with doping and photoexcitation we used the partial sum rule for the effective electron density N_{eff} defined as:

$$N_{eff}(\omega') = \frac{2 \cdot m^* \cdot m_e}{\pi \cdot e^2} \int_0^{\omega'} \sigma_{real}(\omega) d\omega \,,$$

where $\omega'/2 \cdot \pi = 2.2\,THz$ is a cut-off frequency, m_e is the free space electron mass, and m^* is the carrier effective mass. In both cases, photoexcitation lowers the spectral weight N_{eff}/m^* calculated according to the sum rule, indicating either a reduction of N_{eff} or an increase in m^* after absorption of optical pumping.

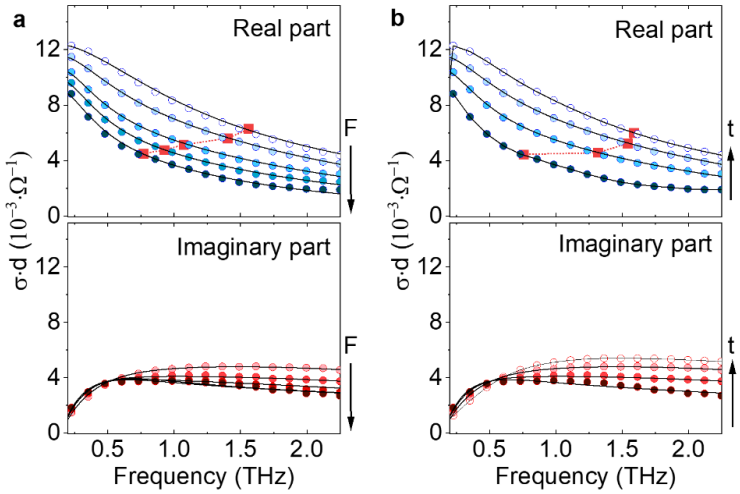

Figure 4.1.2-1. (a) Equilibrium conductance (empty dots) and conductance at $t = 2\,ps$ after excitation (filled dots) of the pristine SWCNT film at laser fluences of $F = 0,\ 2.8,\ 6.95,\ 14.3,\ 26\,\mu J/cm^2$. Real (blue circles) and imaginary (red circles) parts of the measured sheet conductances ($\sigma \cdot d$) are plotted. The arrow F indicates the fluence change from low to high values. Red filled squares connected by a red dotted line indicate a change in the peak width f_{HWHM}. (b) The conductance at $t = 1.8,\ 3.2,\ 5.4,\ 20\,ps$ after photoexcitation, for $F = 26\,\mu J/cm^2$. The arrow t points from early to late times.

The sum rule analysiss provides the carrier sheet density in equilibrium (for pristine SWCNT films), which varies from $2.4 \cdot 10^{14}\,cm^{-2}$ for the pristine sample to $1.2 \cdot 10^{15}\,cm^{-2}$ for the highest adsorption doping case, corresponding to the interval between 1,000 and 5,000 free charges per SWCNT (assuming $m^* = 1$). However, if a lower effective mass more typical of these nanotubes is assumed ($m^* = 0.2$) the value will be between 200 and 1,000 free charges per

SWCNT. Assuming the average SWCNT length of 1 μm, the hole density per unit length is between 1 and 5 nm^{-1} for the highest p-type doped sample. This is comparable to the number of dopant ions per unit length. Since the exciton and hole number density are both high, there is a ready supply of free charges close to each exciton at each SWCNT, satisfying condition of a free charge within the exciton diffusion length (the distance it can travel, on average, before recombination), which can exceed 100 nm in SWCNTs [71–74]. Looking deeper, the pump-probe laser fluence varied along with the detection time as these variables are proportional to the scattering rate of the Drude-Lorentz model which predicts an inverse proportion between the peak width (f_{HWHM}) and the scattering rate (*i.e.* with the increase of the fluence the number of free charge carriers increases, which leads to the collision frequency rise and therefore to the change in f_{HWHM}).

The prominent negative photoconductivity can be seen in Figure 4.1.2-1 comparing the real part of the sheet conductance ($\sigma \cdot d$) of the pristine film without excitation (empty blue circles) and 2 ps after photoexcitation at several pump fluences (filled blue circles). The observed conductivity after photoexcitation was lower in amplitude, and the enhanced suppression of $\sigma_{real}(\omega, t = 2\ ps)$ (the main partial sum parameter) with the increasing fluence is evident in Figure 4.1.2-1a. A higher fluence resulted in a progressively narrowing of $\sigma_{real}(\omega, t = 2\ ps)$, as can be seen for instance from the frequency f_{HWHM} at which the conductivity is half its maximum value (red filled squares in Figure 4.1.2-1). At later pump-probe delays, the conductivity was rapidly recovered back towards its equilibrium level, increasing in amplitude and broadening in width, as shown in Figure 4.1.2-1b. It should be noted that the THz peak of the conductivity is assumed to be located out of the used bandwidth as the maximum value was 0.1 THz (also, the Drude term is rising as the doping level increases and its maximum is assumed to be in *GHz*-region according to the previous works [63,64,69]).

Another important parameter found is the effect of doping on recombination dynamics. To elucidate the origin of negative photoconductivity (positive modulation depth $\Delta E/E$), we obtained N_{eff}/m^* and f_{HWHM} from $\sigma_{real}(\omega, t)$ spectra at pump-probe delays from $t = -2.5$ to 17.5 ps, as reported in Figure 4.1.2-2 for the 15 mM doped sample and the pristine SWCNT film at a fluence of 26 $\mu J/cm^2$. At zero pump-probe delay, N_{eff}/m^* is rapidly suppressed for both the doped and pristine samples. The larger relative reduction in N_{eff}/m^* for the doped sample is the result of its higher absorbance at the pump wavelength. After zero pump-probe delay, N_{eff}/m^* recovers rapidly to its equilibrium level. Solid red lines illustrate fits using $N_{eff}/m^*\,(t) = A - B \cdot e^{-t/\tau}$, where A is the equilibrium value of N_{eff}/m^* and B is the modulation depth. The

recombination times obtained are $\tau = 2.4\ ps$ for the pristine SWCNT film and $\tau = 1.5\ ps$ for the doped film (doped films will react faster in devices). A similar reduction in τ for increasing p-type doping was observed for the gated device. These numbers are close to the 2.7 ps single-exponential trion lifetime reported for hole-doped SWCNTs [71,75–78]. It is shown that trions in polymer-wrapped (6,5) semiconducting SWCNTs are formed within 500 fs of photoexcitation due to the rapid exciton diffusion into less-mobile holes, and then decay with a lifetime of 2 ps. Therefore, the recovery times observed here correspond with trion decay times, which are similar to exciton lifetimes.

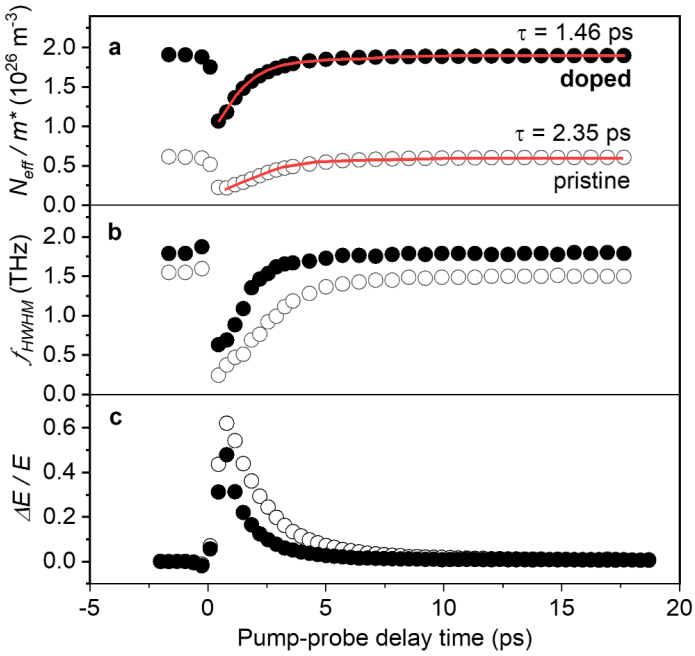

Figure 4.1.2-2. (a) The ratio of effective density of electrons to the effective mass N_{eff}/m^* *vs.* pump-probe delay time t for pristine (open circles) and 15 mM doped (filled circles) samples. Solid red lines illustrate fits using $N_{eff}/m^*(t) = A - B \cdot e^{-t/\tau}$, where A is the equilibrium value of N_{eff}/m^* and B is the modulation depth. (b) Frequency width f_{HWHM} of $\sigma_{real}(\omega, t)$ *vs.* t. (c) $\Delta E/E$ at the peak of the THz pulse *vs.* t.

The momentum scattering rate is also modified dynamically during the recombination process, lowering after photoexcitation and recovering with the same timescale as N_{eff}/m^*, as illustrated in Figure 4.1.2-2b. As with the fluence-dependent data, $f_{HWHM} \propto N_{eff}/m^*$ (if the the corresponding data of pristine and doped in Figure 4.1.2-2a,b is divided one over another the linear dependence can be seen). The doped sample has a shallower gradient than the pristine

sample, implying that the carrier scattering rate is a function of the chemical potential.

Figure 4.1.2-2c also show the $\Delta E/E$ dependence obtained at the peak of the THz pulse, for different pump-probe delays t. The photoinduced THz modulation depth exceeds $\Delta E/E = +60\%$ for the pristine sample when pumped at fluence $F = 26\,\mu J/cm^2$. This suggests a potential application of the giant negative photoconductivity of SWCNTs in ultrafast THz modulators.

This modulation is greater than the depth obtained earlier by positive photoconductivity in GaAs nanowires ($\Delta E/E = -15\%$ for 14 stacked and co-aligned layers, $F = 280\,\mu J/cm^2$) and polymer-wrapped SWCNTs ($\Delta E/E < -0.2\%$, $F = 175\,\mu J/cm^2$). The modulation depth for negative photoconductivity in our SWCNT films is larger than that for MoS_2 ($\Delta E/E = 1.5\%$, $F = 50\,\mu J/cm^2$) and graphene ($\Delta E/E = 3\%$, $F = 50\,\mu J/cm^2$).

Here, the high THz conductivity of the film was efficiently modulated by the strong optical absorption of the SWCNTs, giving high modulation depths while maintaining an ultrafast decay time, which was tuned by changing the doping level. At higher fluences the changes in N_{eff}/m^*, f_{HWHM}, and $\Delta E/E$ appear to be saturated, potentially as a result of the bleaching of the excitonic absorption resulting in an average of less than one exciton per incident photon.

Overall, the observation of negative photoconductivity for pristine and doped SWCNT films demonstrates that it is an intrinsic property of SWCNT thin films and that it occurs for all doping levels. This observed negative photoconductivity effect was caused by a photo-induced lowering of the free charge density (or increased mass), which is ascribed to the formation of trions, and which simultaneously lowered the momentum scattering rate. The high THz conductivity obtained for both pristine and doped films is attributed to the high mobility and long conductivity length of aerosol-synthesized films, as well as effective doping. Finally, the negative ultrafast photoconductivity (leading to giant modulation depth, broad bandwidth, and picosecond switching speeds) reported here offers significantly greater modulation depths (reaching $\Delta E/E > 60\%$) than that obtained at the same pump fluences in alternative materials, opening new prospects for designing of ultrafast spectrally wide-band THz TCF-based devices using pristine and doped randomly oriented and large-scale SWCNT films.

4.2 Adsorption doping

The goal of this chapter is to elaborate simple approaches appropriate for high-volume production of high-conductive TCFs based on large-scale SWCNT films (Publications I, II, V). The outcomes introduced here provide simple and straightforward techniques to achieve the state-of-the-art results.

4.2.1 Hybrid SWCNT/graphene film

We report a novel, scalable and commercially feasible process for the fabrication of hybrid SWCNT-graphene TCFs using aerosol-synthesized SWCNT films and commercially available graphene oxide solutions. First, the SWCNT film is deposited onto a substrate, then a thin layer of graphene oxide is deposited on top of the SWCNT film via spray deposition. The next step is the reduction of GO, followed by adsorption doping of the hybrid with $AuCl_3$. This method yields TCFs with the state-of-the-art equivalent sheet resistance value of $R_{90} = 73\ \Omega/\square$ (recalculated from as-measured data of $R_S = 35\ \Omega/\square$ and $T_{550} = 80\%$).

For the selection of an optimal temperature of the substrate, graphene oxide was deposited on conductive aluminum substrates and the resulting samples were analyzed using SEM. The distance between the airbrush and the substrate, as well as the feed rate, were kept constant. At lower temperatures, such as 100 and 125 $°C$, the droplets are agglomerating and the resulting droplet size is more than 100 μm. This leads to highly non-uniform coverage of the substrate with GO sheets. When the substrate is heated to 250 $°C$ and higher, the water evaporates before the droplet reaches the substrate. Consequently, GO sheets, that tend to stay within the droplet, become crumpled, and form 3D structures on the substrate surface. This is unacceptable for the SWCNT-graphene hybrids for TCFs since for better performance the graphene sheets have to form a flat layer on top of SWCNTs.

One more phenomenon can be noticed at temperatures of 200 to 250 $°C$: so-called “coffee rings”, ring-like stains along the droplets’ contact lines, start forming. This was explained by the higher liquid evaporation rate at the droplet’s edge. The formation of coffee rings leads to non-uniform distribution of GO flakes on the substrate’s surface and is, therefore, detrimental to the material’s conductivity. Considering all of the above, substrate temperatures of 150 to 200°C were considered optimal for graphene oxide spray deposition. In this range, the GO sheets are distributed uniformly on the substrate surface. Further experiments were carried out with the substrates heated to 200°C (Figure 4.2.1-1).

Two methods for GO reduction were evaluated in this study: ambient atmosphere reduction and H_2 reduction. Even though full reduction of GO cannot be achieved by heating in the ambient atmosphere, this method is low-cost, fast and does not require special equipment or use of hazardous chemicals. During ambient atmosphere reduction, partially oxidized carbon is transformed into CO_2 and fully reduced graphene. The following parameters were identified to be important for the thermal reduction at ambient conditions: 1) temperature, 2) treatment time. These two parameters have the opposite effect on the thermal reduction of GO: the higher the temperature, the lower is the treatment time required for maximum achievable reduction. A series of

experiments were therefore performed at a fixed temperature of $200\,°C$ with treatment times varied from 0.5 to $32\,min$ (see supplementary material). The contact angle (or wetting angle as a measure of the wettability of a solid by a liquid) [79], θ, and the transmittance change, ΔT, were used to evaluate the degree of reduction of the GO films. The contact angle increases until the treatment time of $8\,min$ is reached and starts decreasing after $8\,min$. This behavior likely indicates that at $200\,°C$, oxidation starts to progress at annealing times longer than $8\,min$. The maximum contact angle achieved during the thermal annealing at the ambient atmosphere is 58°, which is significantly lower than the anticipated contact angle for water on graphene of $90 \div 100°$. The temporal evolution of the transmittance change shows that at $t = 8\,min$ transmittance stops decreasing. Therefore, the reduction time of $8\,min$ was considered to be optimal for the thermal reduction at the ambient atmospheric treatment at $200\,°C$.

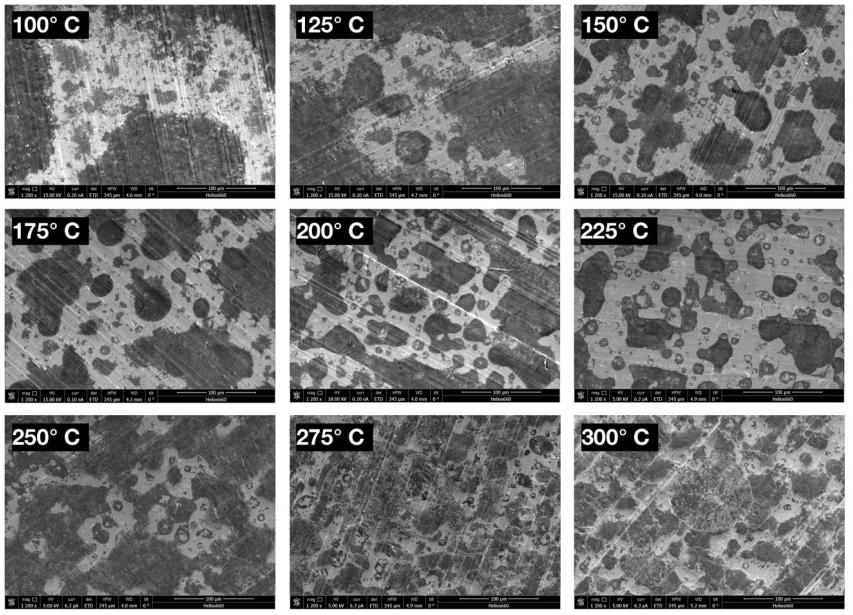

Figure 4.2.1-1. The effect of substrate temperature on the morphology of spray-deposited graphene oxide films: SEM micrographs of GO on aluminum. Low substrate temperatures ($100 \div 125\,°C$) correspond to non-uniform coverage of the substrate, high substrate temperatures ($250 \div 300\,°C$) correspond to crumpling of GO sheets. Temperatures of $150 \div 200\,°C$ are considered optimal for GO deposition.

The mean sheet resistance of hybrid SWCNT/rGO films obtained by ambient atmosphere reduction is lower than that of SWCNT-only films ($R_S = 302\,\Omega/\square$ for hybrids and $R_S = 368\,\Omega/\square$ for SWCNT films), their equivalent resistance is higher due to the decrease in transmittance. It can be concluded that the degree

of reduction (and the resulting increase in conductivity) achieved by ambient atmosphere reduction is not enough to account for the decrease in optical transmittance. The performance of these films was further improved by adsorption doping.

Thermal annealing in the H_2 atmosphere was performed for samples with various SWCNT and GO film thicknesses. Similarly to ambient atmosphere reduction, the quality of hybrid materials depends on the annealing time and annealing temperature. An XPS study was performed to compare the reduction quality for the samples reduced in H_2 and at ambient atmosphere. Survey O 1s and C 1s XPS spectra are presented in Figure 4.2.1-2. C 1s spectra show that the SWCNT-GO sample contains the biggest amount of oxygen-containing carbon bonds. The amount of oxygen-containing bonds is significantly lower in the sample that was reduced in an ambient atmosphere. The sample that reduced in H_2 has the lowest amount of carbon-oxygen bonds, which suggests that this method is more effective at removing oxygen-containing functional groups and reducing graphene oxide. The results of the XPS studies are in agreement with the analysis of optoelectronic performance of the samples. The test samples produced by annealing in H_2 atmosphere demonstrate lower equivalent sheet resistance difference ($R_{90}^{before\ doping} - R_{90}^{after\ doping}$): their mean value is $264\ \Omega/\square$, while the samples reduced in air had a mean value of $485\ \Omega/\square$.

The structure of the SWCNT-rGO hybrids was characterized using SEM and TEM (Figure 4.2.1-3). The ED pattern (inset in Figure 4.2.3.2c) shows five hexagonal patterns and, therefore, confirms that graphene layers are overlapped. SEM imaging of the scratched hybrid sample reveals that the rGO sheets form a thin, uniform layer on top of the SWNT films (Figure 4.2.1-3d).

As the samples were produced, we applied the doping procedure to them to achieve SWCNT/rGO hybrids.

The doping with $AuCl_3$ was performed for all hybrid samples. The results of doping in terms of optoelectronic performance of the samples are presented in Figure 4.2.1-4. Both sheet resistance and transmittance of the samples decrease significantly after the $AuCl_3$ doping. Despite the decrease in the transmittance, an equivalent sheet resistance of the doped samples is significantly lower: median equivalent resistance for all samples before doping is $R_{90} = 567\ \Omega/\square$, after doping – $R_{90} = 108\ \Omega/\square$, which constitutes a 5-fold decrease in the equivalent sheet resistance.

The doping results are different for the samples that reduced in H_2 and for those that were reduced in the ambient atmosphere (Figure 4.2.1-4). Even though XPS studies show that H_2 reduction was more effective at reducing GO, the samples produced by this method demonstrate higher equivalent resistance after $AuCl_3$ doping (Figure 4.2.1-4c). The mean R_{90} of the samples produced by annealing in H_2 and $AuCl_3$ doping is $138\ \Omega/\square$, while the mean R_{90} of the

samples produced by ambient atmosphere reduction and $AuCl_3$ doping is 98 $\Omega/\square$. This effect can be attributed to the fact that during H_2 reduction some of the structural defects are being repaired. The resulting SWCNT/rGO hybrids have better optoelectronic performance but are significantly less susceptible to adsorption doping.

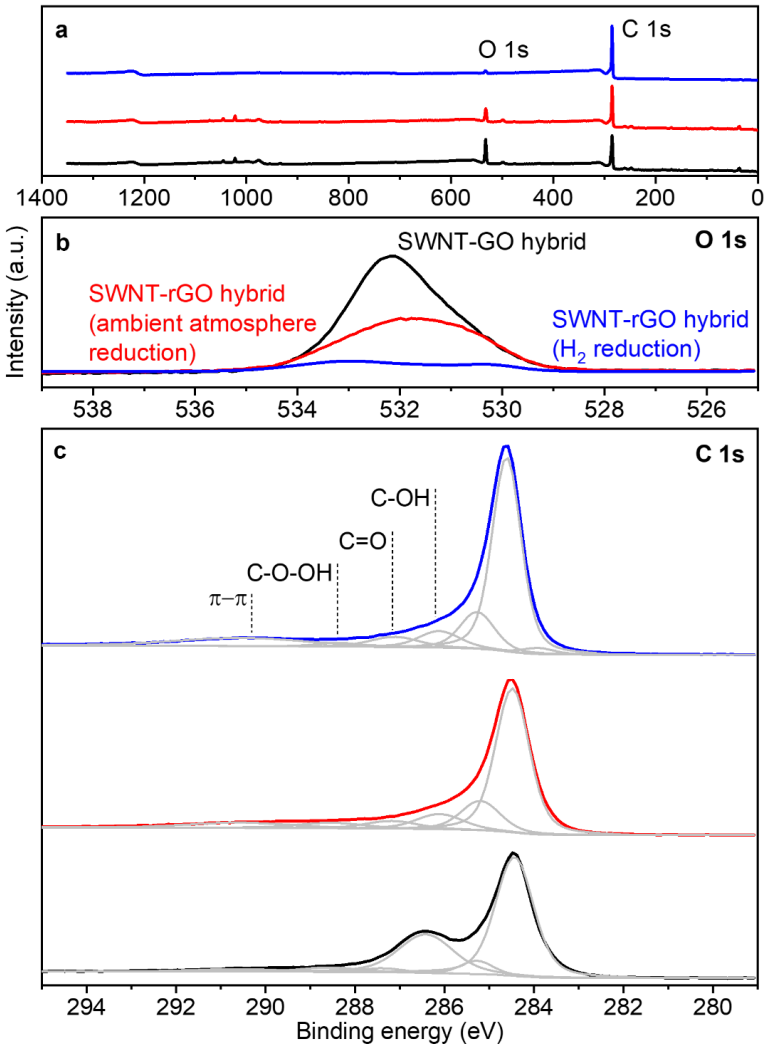

Figure 4.2.1-2. XPS spectra of SWCNT-GO and SWCNT-rGO hybrids. (a) Comparison of XPS survey spectra of SWCNT-GO, SWCNT-rGO (reduced in ambient atmosphere) and SWCNT-rGO (reduced in H_2) hybrids, (b) O 1s XPS spectra of SWCNT-GO, SWCNT-rGO (reduced in ambient atmosphere) and SWCNT-rGO (reduced in H_2) hybrids, (c) C 1s XPS spectra of SWCNT-GO and SWCNT-rGO hybrids. The sample that was annealed in H_2 atmosphere has the lowest amount of carbon-oxygen bonds, which suggests that this method is more effective at removing oxygen-containing functional groups and reducing graphene oxide.

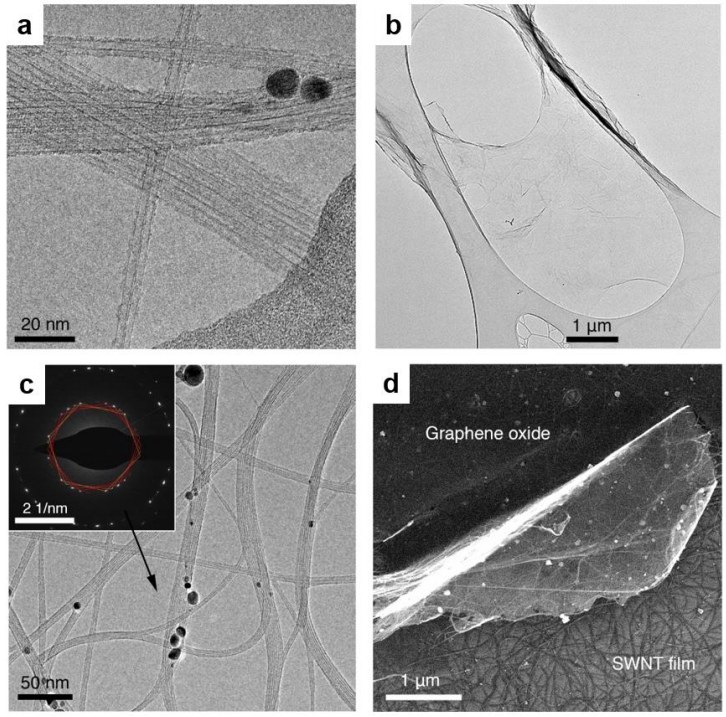

Figure 4.2.1-3. (a) TEM micrograph of an SWCNT film, (b) TEM micrograph of rGO film, (c) TEM micrograph of SWNT/rGO hybrid with an ED pattern, taken from the rGO area and showing the mismatch in graphene layers, (d) SEM micrograph of the scratched surface of the SWCNT/rGO hybrid.

The best optoelectronic performance achieved in this work is $R_{90} = 73\ \Omega/\square$ obtained for an as-measured sample of $R_S = 35\ \Omega/\square$ and $T_{550} = 80\%$. This sample was acquired by ambient atmosphere reduction and subsequent $AuCl_3$ doping. This film demonstrates significantly improved optoelectronic performance as opposed to SWCNT-only film ($R_{90} = 440\ \Omega/\square$), $AuCl_3$-doped rGO film ($R_{90} = 12.2\ k\Omega/\square$) or $AuCl_3$-doped SWCNT film ($R_{90} = 127\ \Omega/\square$). Compared with optoelectronic performance of CNT/graphene hybrids reported in the literature (Figure 4.2.1-5), the samples produced in this work also show superior performance: Bittolo Bon and coworkers achieved R_{90} of $409\ \Omega/\square$ [80], Kholmanov *et al.* — $291\ \Omega/\square$ [81], Tung *et al.* — $344\ \Omega/\square$ [82].

The optoelectronic performance of the fabricated SWCNT/rGO hybrids this work is already better than the performance of ITO on PET substrate and satisfies most of the requirements for device electrodes.

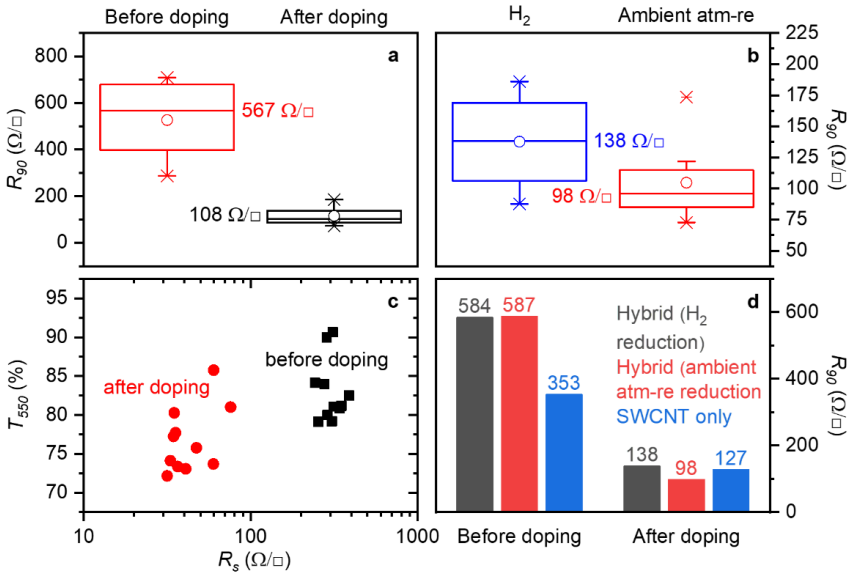

Figure 4.2.1-4. Effect of $AuCl_3$ doping on SWCNT/rGO hybrids: (a) Median equivalent resistance before doping is 567 $\Omega/\square$, after doping – 108 $\Omega/\square$ which constitutes a 5-fold decrease in equivalent resistance, (b) $AuCl_3$ doping is significantly more effective for the samples that were reduced in ambient conditions: these samples demonstrate lower equivalent resistance after doping than the samples that were reduced in hydrogen, (c) hybrid SWCNT-rGO films demonstrate significantly lower resistance after $AuCl_3$ doping, (d) comparison of equivalent resistance of SWCNT-only films and SWCNT-rGO hybrids before and after doping with $AuCl_3$.

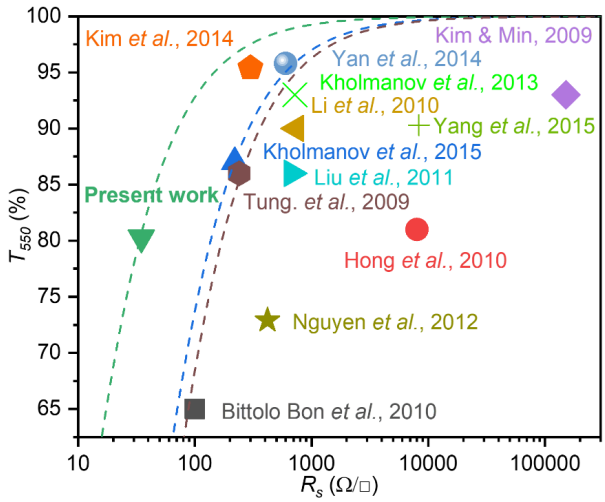

Figure 4.2.1-5. Comparison of optoelectronic performance of SWCNT/graphene hybrids reported in the literature and in present work. Dashed lines indicate the theoretical relationship between optical transmittance at 550 nm (T_{550}) and sheet resistance (R_S) and can be used to calculate equivalent sheet resistance (R_{90}).

The optoelectronic performance of SWCNT/rGO hybrids obtained by the method introduced in this work can be further improved. One way to increase conductivity without sacrificing the transmittance of a film is using monolayer GO (or graphene) flakes. Another route is to choose a GO deposition method that allows for uniform distribution of GO flakes on SWCNT film, *e.g.* Langmuir-Blodgett assembly. Moreover, using GO with large flakes might yield films with better conductivity.

4.2.2 Solvent optimization procedure

Aiming at the goal of obtaining the most conductive films, we carried out preliminary investigations to select the most effective dopant among $AuCl_3$ and $HAuCl_4$ (chloroauric acid). The results of the UPS measurements are summarized in Table 1 in Publication I. Briefly, the work function of the films increased from $4.46\ eV$ (for pristine SWCNTs) to $5.87\ eV$ (for $AuCl_3$-doped SWCNTs) and $6.14\ eV$ ($HAuCl_4$-doped SWCNTs) for the $T_{550} = 80\%$ film. Thus, the doping by $HAuCl_4$ decreased the E_F in the SWCNTs by almost $1.7\ eV$, which is about $0.3\ eV$ more than in the presence of $AuCl_3$. Similar results were obtained for the $T_{550} = 65\%$ films (Table 1 in Publication I). Based on the aforementioned findings, we used $HAuCl_4$ for our further doping studies.

The results of the optical characterization of the $T_{550} = 90\%$ films are presented in Figure 4.2.2-1a. UV-Vis-NIR transmittance spectra of the pristine and $HAuCl_4$-doped samples revealed respective T_{550} changes from 90% to 87%. The decrease in T_{550} after the doping occurs due to the formation of gold NPs on the surface of SWCNTs, which could be proven on a basis of the existence of Au NP surface plasmon resonance peaks in the region of $190 \div 400\ nm$ [28,31,83,84]. Raman spectra of the pristine SWCNTs (Figure 4.2.2-1b) confirms their high quality with the G- to D-band intensity ratio of $I_G/I_D = 130$. After the doping with $HAuCl_4$, new Raman peaks appeared at the region of $310 \div 370\ cm^{-1}$. These peaks revealed the formation of the Au-Cl stretching region peaks [84] related to different gold complexes. The TEM micrograph of pristine SWCNTs shows the morphology of randomly oriented individual and small bundled SWCNTs (Figure 4.2.2-1c). The $HAuCl_4$-doped SWCNTs reveal the formation of amorphous "skin" of the dopant on the surface of the nanotubes (Figure 4.2.2-1d).

For our comparison experiments, we selected solvents, which can dissolve gold chloride [85], and investigated the effect of their properties on the SWCNT doping results. The variety of the physicochemical properties of the model solvents, namely saturated vapor pressure at room temperature, viscosity, surface tension, and boiling temperature, is shown in Figure 4.2.2-2. From the listed parameters of the solvents (tetrahydrofuran (THF), ethanol (EtOH),

acetonitrile (ACN), dimethylformamide (DMF), dimethylsulfoxide (DMSO), and n-methyl-2-pyrrolidone (NMP)) the boiling temperature and saturated vapor pressure values were believed to play the most important roles, since they determine the evaporation time of the solvent. The solvents in Figure 4.2.2-2 were arranged according to their boiling temperatures.

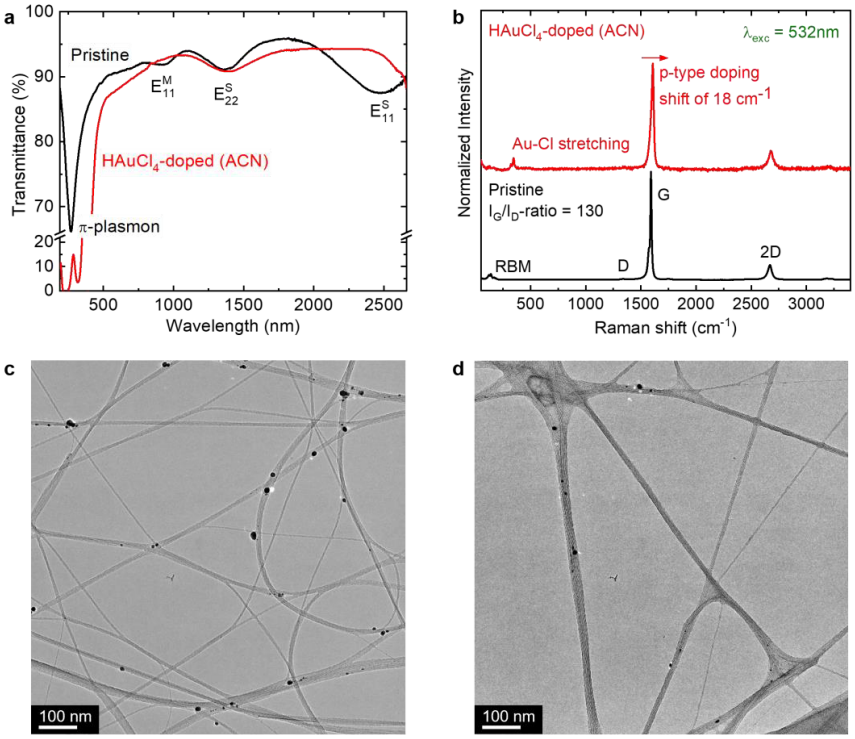

Figure 4.2.2-1. Characterization of pristine and $HAuCl_4$-doped (using acetonitrile (ACN) as a solvent) SWCNT films: (a) UV-Vis-NIR transmittance spectra of pristine (solid black) and $HAuCl_4$-doped (dashed red) SWCNTs; (b) Raman spectra of pristine (solid black) and $HAuCl_4$-doped (solid red) SWCNTs. TEM micrographs of (c) pristine and (d) $HAuCl_4$-doped SWCNTs.

The resulting R_{90} of the $HAuCl_4$-doped samples of $T_{550} = 85\%$ nanotubes for different solvents are shown in Figure 4.2.2-3. The lowest mean value of the equivalent sheet resistance of $R_{90} = 46\ \Omega/\square$ ($K = 475\ 1/k\Omega$) was obtained with THF, EtOH, and ACN. Only EtOH samples showed haze-free morphology, which distinguishes these samples from all others and allows them to be used as TCFs. For a few samples doped using THF, EtOH, and ACN as a solvent the value of R_{90} was found to be as low as $R_{90} = 40\ \Omega/\square$ and this number to the best of our knowledge is the lowest equivalent sheet resistance obtained for SWCNT films [40,86–91]. As can be seen from the Figure 4.2.2-3, THF, EtOH, and ACN allowed to fabricate the films with similar optoelectrical properties, while high boiling temperature solvents (DMF, DMSO, NMP) are inferior in the

performance. DMF, DMSO, and NMP correspondingly led to the R_{90} values of 104, 209, and 206 $\Omega/\square$. It is worth noting that the significant role in the performance can be attributed to the decrease in the transmittance of the doped films (DMF: 41 $\Omega/\square$ and T_{550} = 77%, DMSO: 39 $\Omega/\square$ and T_{550} = 57%, and NMP: 57 $\Omega/\square$ and T_{550} = 69%). In the case of DMSO, its T_{550} value dropped significantly lower and is closely aligned with the formation of the thin gold film [92]. To reveal the role of the solvent for further studies we selected EtOH, ACN, and DMF.

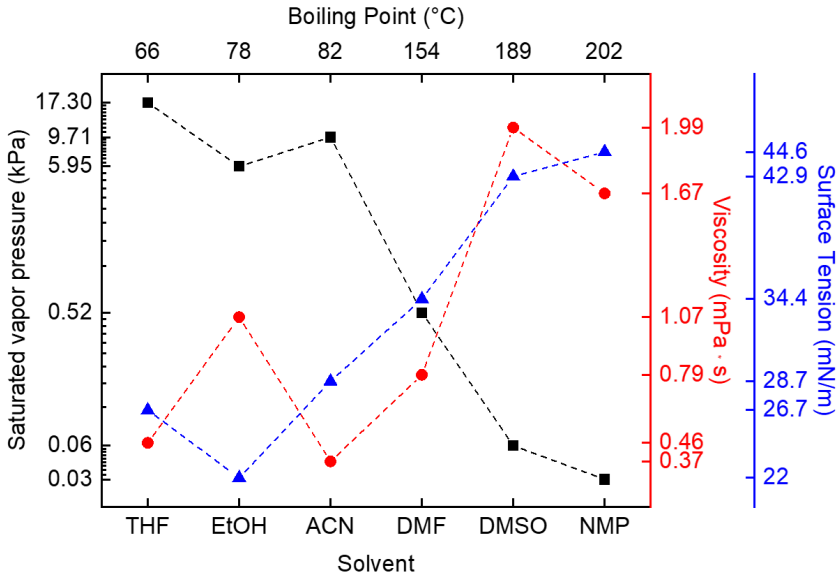

Figure 4.2.2-2. Physicochemical properties of the solvents utilized for the studies: saturated vapor pressure (black squares), viscosity (red circles), and surface tension (blue triangles), and boiling temperatures of the solvents: tetrahydrofuran (THF), ethanol (EtOH), acetonitrile (ACN), dimethylformamide (DMF), dimethylsulfoxide (DMSO), and n-methyl-2-pyrrolidone (NMP). Dashed lines between points serve only as guides for the eye.

First of all, the low R_{90} values of EtOH, ACN, and DMF are accompanied by the presence of several distinguishing features of $HAuCl_4$-doping mechanism in Raman spectra. Among the most useful of them are strong *p*-type doping shift of G-mode [40] and Au-Cl stretching region peaks (Figure 4.2.2-4a) [84,93]. Previous studies of SWCNT doping with $AuCl_3$ and $HAuCl_4$ proposed that the most profound influence on the doping is caused by the presence of $[AuCl_4]^-$ due to the extraction of electrons from SWCNT to the dopant to reduce Au^{3+} ions [31,40,94]. As could be seen from Figure 4.2.2-4a, there are clear Au-Cl stretching peaks, confirming its presence on all doped samples of the SWCNT films. The Au-Cl stretching region consists of two main peaks related to gold chloride bonds (Figure 4.2.2-4a): a high-intensity peak at 347 cm^{-1} $[AuCl_4]^-$

and a low-intensity peak at 324 cm^{-1} $[AuCl_4]^-$. The XPS of pristine and $HAuCl_4$-doped SWCNTs, using ACN as a solvent, also showed the presence of Au and Cl peaks in the doped sample (Figure S2 in Publication I). The position of G-mode of pristine SWCNTs was 1589 cm^{-1}. As can be seen from Figure 4.2.2-4b, the average shift of G-mode was significant for all of the doped samples (about 17 cm^{-1}), which is consistent with the changes observed for the R_{90} data presented in Figure 4.2.2-3.

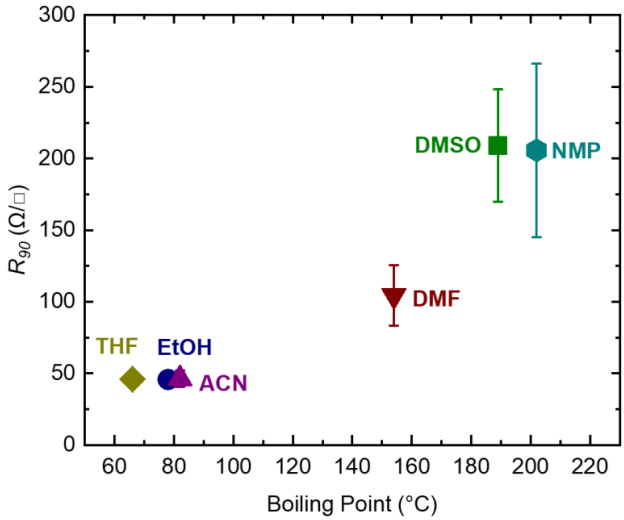

Figure 4.2.2-3. The resulting equivalent sheet resistance R_{90} of the $HAuCl_4$-doped samples at room temperature plotted *vs.* the boiling point temperature of the solvents.

Next, we examined the role of pure solvents on the optoelectrical performance of the SWCNT films. After the collection at the reactor outlet, the aerosol synthesized SWCNTs exist in the form of a wool structure with a low density (Figure S3a in Publication I) and can be densified by treating the film with a liquid (Figure S3b in Publication I) [19]. As a result of the liquid evaporation, due to the surface tension, the film is shrunk into a uniform densified film. To reveal the densification effect on the optoelectronic performance of the films, drop-casting experiments with the pure solvents (without gold chloride) were performed. The electrical and optical measurement results did not show any clear dependence with the solvent nature. Usually, the film densification resulted in a 1% increase in T_{550} and a 30% decrease in R_S. From Raman spectra of the densified samples, no visible changes related to any kind of doping were also detected (Figure S4 in Publication I). Thus, no clear trend or correlation of R_{90} with pure solvent for the bundle restructuring due to densification was observed.

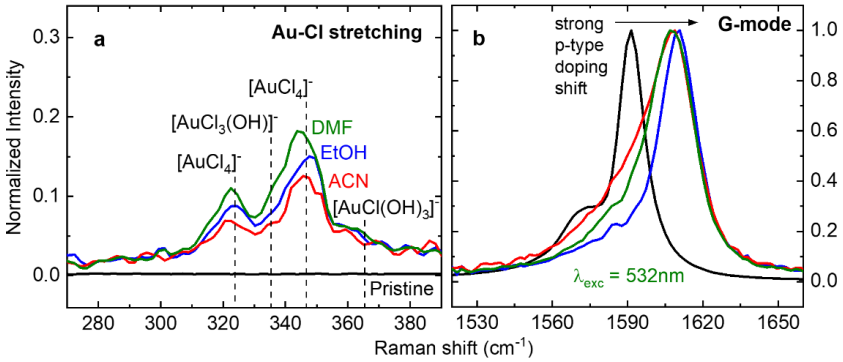

Figure 4.2.2-4. Raman spectra (normalized intensity) of the $HAuCl_4$-doped samples in the region of (a) Au-Cl stretching and (b) G-mode.

Not only evaporation of the solvent and densification might have an effect on the final conductivity of the films, but also the dispersability of the SWCNTs in the solvent can be the limiting parameter to define the optoelectronic performance. We examined Hansen solubility theory, describing and helping to predict solubility and wettability, for a correlation with the experimental data. The theory is based on three Hansen solubility parameters describing the dispersion (δ_D), polarity (δ_P), and hydrogen bonding (H-bonding, δ_H) [95]. The sum of squares of these parameters gives the square of the Hildebrand solubility parameter (δ_T): $\delta_T^2 = \delta_D^2 + \delta_P^2 + \delta_H^2$.

For any system, for better solubility the Hansen parameters of the solute (SWCNTs) and solvent need to be as close as possible, leaving the distance (D) in Hansen space to the minimal value:

$$\mathrm{D} = \sqrt{(\delta_{D,SWCNT} - \delta_{D,solv.})^2 + (\delta_{P,SWCNT} - \delta_{P,solv.})^2 + (\delta_{H,SWCNT} - \delta_{H,solv.})^2}.$$

In our case, the smallest value of D in the ternary space of the Hansen solubility components for SWCNTs was found for THF and NMP (Figure 4.2.2-5a), but among those solvents only THF resulted in a good optoelectrical performance (Figure 4.2.2-3). At the same time, it is known that NMP is one of the best dispersants for SWCNTs. As can be seen, no correlation with the best R_{90} values for EtOH and ACN could be found. This could point out that wetting and swelling of the SWCNTs are not the most crucial parameters in the SWCNT film conductivity enhancement.

In general, we could not find any clear correlation of the optoelectronic performance with the Hansen solubility parameters, but with the dispersive component (Figure 4.2.2-5b-d). As one can see from Figure 4.2.2-5b, a similar trend was observed between R_{90} *vs.* δ_D and the results presented in Figure 4.2.2-3 for R_{90} *vs.* boiling temperature of the solvents. It is known that the dispersive component is determined by non-polar interactions derived from atomic and molecular attractive forces. These forces have temperature-dependent nature

and therefore among other properties determine the boiling temperature and saturated vapor pressure of the solvent. Thus, from the dependence of the equivalent sheet resistance on solvent and its relation to dispersive component (Figure 4.2.2-3 and Figure 4.2.2-5b) could be concluded that the most significant factor in the doping process is the solvent evaporation rate.

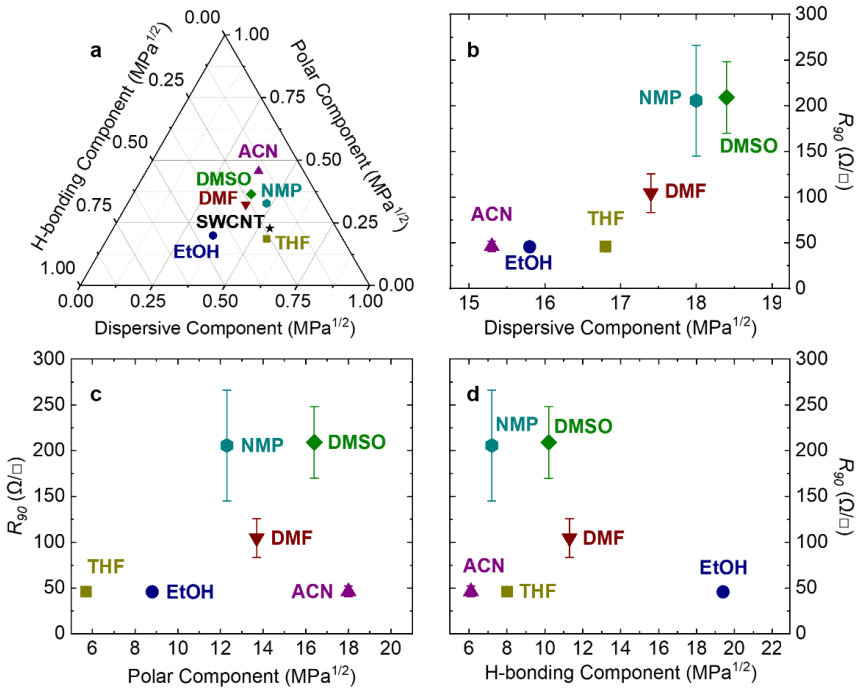

Figure 4.2.2-5. (a) Ternary plot of SWCNTs and the solvents used for the study *vs*. Hansen solubility components at room temperature: dispersive, polar, and H-bonding component. Equivalent sheet resistance (R_{90}) *vs*. (b) dispersive, (c) polar, and (d) H-bonding components.

As for the temperature effect on doping, it is worth noting that after the drop-casting on SWCNT films, the complete evaporation of the solvent (the solution droplet size was 20 μL) with $HAuCl_4$ dissolved might take from a second to the whole day for various solvents. The longest times to evaporate at room temperature were observed for DMF, DMSO, and NMP: about 47 *min*, 24 *hours*, and 26 *hours*, correspondingly, while THF, EtOH and ACN drop-casting resulted in only 2 *min* evaporation.

One can propose that for the high boiling-temperature solvents to get better optoelectrical results, we need to accelerate the evaporation of the solution and therefore to heat them up. To illustrate the influence of the solvent evaporation rate on the equivalent sheet resistance, we carried out a series of doping experiments at different temperatures (Figure 4.2.2-6). This approach was applied to examine the effect on the equivalent sheet resistance values of the

previously selected solvents: EtOH, ACN, and DMF. The lowest mean values of $R_{90} = 46\ \Omega/\square$ (corresponding to $K = 475\ 1/k\Omega$) were obtained for EtOH and ACN at room temperature. For DMF, the best results were observed at 40 ℃ with $R_{90} = 69\ \Omega/\square$ corresponding to $K = 317\ 1/k\Omega$ (Figure 4.2.2-6c). When the temperature was increased to 40 ℃ the evaporation time has decreased from 45 to 20 min. Unfortunately, we have not observed the further improvement of the equivalent sheet with temperature. This most likely can be explained by the environmental effect of de-doping due to the hygroscopic nature of gold chloride and is accomplished with the release of chlorine and reduction of gold ions on the surface of SWCNTs [28,31,40]. The evolution of the gold NPs formed at room temperature and 80 ℃ is shown in Figure 4.2.2-7. As can be seen from the figure, the higher temperature results in the larger diameter of gold NPs and higher particle concentration. Therefore, SWCNTs become decorated with gold NPs, which affects the optoelectrical properties of the fabricated TCFs by reducing its transmittance.

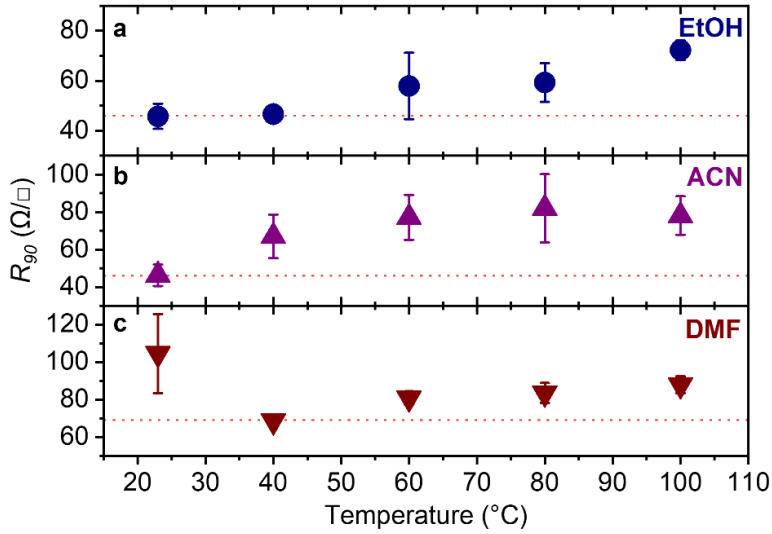

Figure 4.2.2-6. Comparison of the temperature T (at which the doping is performed) dependence of the equivalent sheet resistance R_{90} of $HAuCl_4$-doped SWCNTs. The dopant dissolved in different solvents: (a) EtOH, (b) ACN, and (c) DMF. The red dotted line is associated with the lowest value obtained for a particular solvent.

When compared with optoelectronic performance of the *p*-type doped SWCNTs reported in literature (Figure 4.2.2-8), the samples produced in this work show superior performance which is already better than the performance of ITO on PET substrates [86–91,96] and satisfies most of the requirements for device TCFs [18,20,35,86–91,96–100]. To improve the mentioned stability

issue, poly(3,4-ethylenedioxythiophene) (PEDOT) and related polymers can be used to cover and protect doped SWCNTs from the environment [94].

The method of the SWCNT doping presented in this work also allows obtaining highly conductive and transparent films on flexible substrates. Figure 4.2.2-8b shows the $HAuCl_4$-doped SWCNT film transferred on a PET substrate. We should notice that the equivalent sheet resistance formula for the thick and thin nanotube is not the same (Figure 4.2.2-8), which can be attributed to the densification effect dependence on the thickness and related to it scattering.

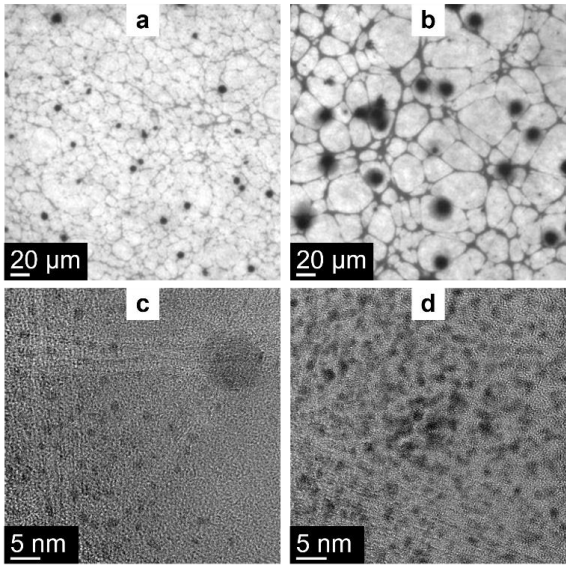

Figure 4.2.2-7. TEM images of the $HAuCl_4$-doped (using ACN as a solvent) samples at (a, c) room temperature and (b, d) 80 °C.

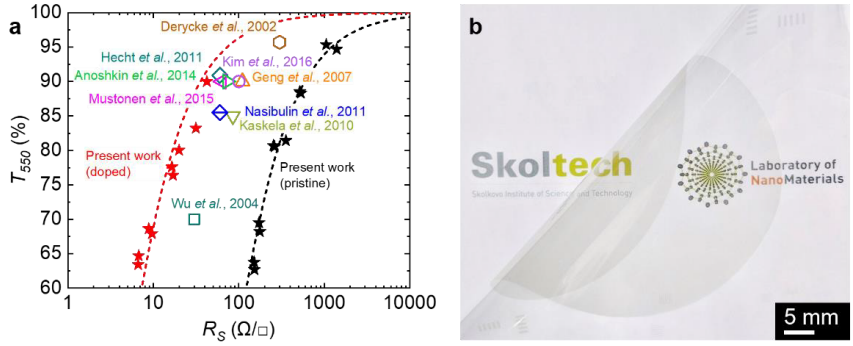

Figure 4.2.2-8. Comparison of the optoelectronic performance of SWCNT-based TCFs after *p*-type doping: sheet resistance R_S *vs.* optical transmittance T_{550}. Dashed lines indicate the theoretical relationship between transmittance and sheet resistance of pristine (black) and $HAuCl_4$-doped (using EtOH as a solvent) SWCNT films (red) obtained in this work. (b) A photograph of an $HAuCl_4$-doped SWCNT film on a flexible PET substrate.

4.2.3 Fine-tuning of optoelectronic performance

To increase the conductivity of the SWCNTs, usually, one of three methods of doping is utilized: drop-casting, spin-coating or dip-coating [101,102]. Although these techniques allow to significantly decrease sheet resistance of pristine SWCNT films (up to 15 $times$) [103], they lack the spatial uniformity and scalability due to non-uniform evaporation of liquid solvent leading to coffee-ring effect [101]. Moreover, none of the methods allow to precisely control the E_F in the SWCNTs.

Here, we propose a novel technique to dope SWCNT films in a controlled manner by employing liquid aerosol particles (droplets) containing a dopant dissolved in a volatile solvent. By varying the aerosol deposition time, we carefully control the work function and sheet resistance of SWCNT films. We believe that the method proposed allows to open a new avenue for fine-tuning of the electronic structure of low dimensional materials for optoelectronics not only to replace the existing ITO electrodes, but also to develop novel applications of highly conductive, flexible, and transparent films.

For our experiments, we utilized high-quality films of randomly oriented SWCNTs produced by the aerosol (floating catalyst) CVD method [8]. We employed thin SWCNT films with T_{550} of 50 and 85% as the model samples. The as-synthesized SWCNT films were dry transferred onto a required substrate (usually quartz or PET; a free-standing configuration was obtained by transferring the SWCNT films over an opening in the substrate [20]) for dopant deposition and further characterization. The detailed description of the experimental setup is presented in extensively discussed in Publication II. Concisely, one of the most effective *p*-type dopants, namely tetrachloroauric (III) acid trihydrate ($HAuCl_4 \cdot 3H_2O$; ACROS Organics), was dissolved in ethanol (C_2H_6O; 99.5%, ETAX) at the concentration of 3.75 or 7.50 mM and aerosolized by OMRON compressor nebulizer NE-C801 (Figures 4.2.3-1 and Figure 3.3-1). The aerosol was transferred with the air flow of 6 l/min through a tube with a diameter of 12 mm and deposited on top of SWCNT films. Ethanol droplets (~11 μm in size, as estimated from the NSD measurements and traces on the films in Figure S2 and S3 of Publication II) were deposited on the surface of SWCNTs. The droplets impregnate the SWCNT films with the subsequent ethanol evaporation, leaving a $HAuCl_4$ coating on the surface (Figure 4.2.3-2). It is worth mentioning that the droplets of the dopant solution after the complete solvent evaporation form aerosol residue particles [104,105] with the diameter of 70 nm as measured by scanning mobility particle sizer spectrometer (Model 3938, TSI) and described in details in Publication II (Figure S2 and S3 in Publication II). Briefly, the quantity of the dopant was estimated to be in a good agreement with the $HAuCl_4$ amount in one droplet deposited on the film.

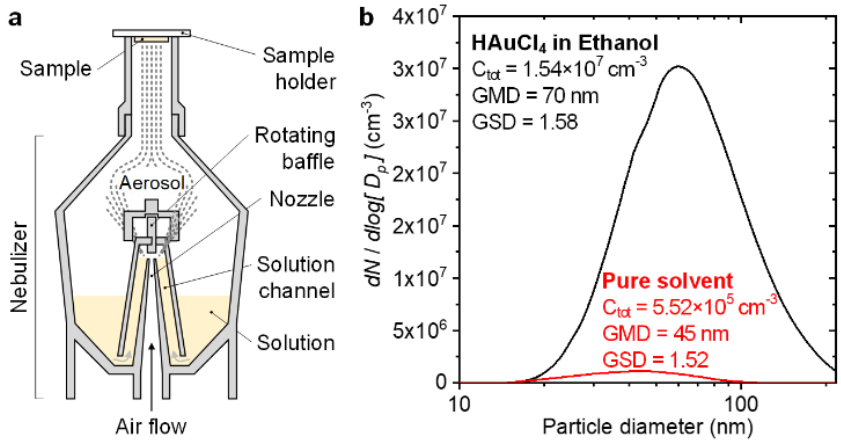

Figure 4.2.3-1. The experimental setup used for the aerosol doping of SWCNT films by 11 μm-sized droplets. (b) The number size distribution of residue aerosol particles left after evaporation of pure ethanol (red) and solution of $HAuCl_4$ in ethanol (black). Total concentration (C_{tot}), geometric mean diameter (GMD), and geometric standard deviation (GSD) are presented for each of the distribution.

Figure 4.2.3-2 shows scanning (SEM, HR-SEM Merlin, Zeiss) and transmission (TEM, Tecnai G, FEI) electron microscopy images of the samples of pristine and doped SWCNTs. Considering the morphology evolution with the doping time, we achieved a more densified film for the highly doped sample (Figure 4.2.3-2a) as well as larger coating and filling with Au NPs across the film (Figure 4.2.3-2b, c).

As was previously shown, $HAuCl_4$ is one of the most efficient dopants for SWCNTs, which shifts the E_F deeper into the valence band [103]. The shift mainly depends on the concentration of the dopant appeared on the surface of SWCNTs. Therefore, increasing the deposition time (1.5, 9.0, and 1050 s) results in a higher doping level in the SWCNTs, which can be observed in a smooth spectral change with the doping time in the UV-Vis-NIR (Figure 4.2.3-3a-e) and Raman (Figure S3a-d in Publication II) spectra, measurements of sheet resistance and work function of the films (Figure 4.2.2.3g,h). Increasing the doping time results in the decrease of R_S from 79 to 3.2 $\Omega/\square$ for the SWCNT films with $T_{550} = 50\%$. The mentioned increase in the conductivity is consistent with the work function rise from $\Phi_{0.0} = 4.45\ eV$ for the pristine nanotubes to $\Phi_{1050} = 5.46\ eV$ for the doping time of 1050 s (Figure 4.2.2.3f). The dramatic changes in R_S (24.5 times higher compared to the pristine values) can be explained by the efficient doping method and attributed to both: the reduction of Schottky barrier height between the metallic and semiconducting nanotubes [106] and increase in the concentration of charge carriers in the SWCNTs [19].

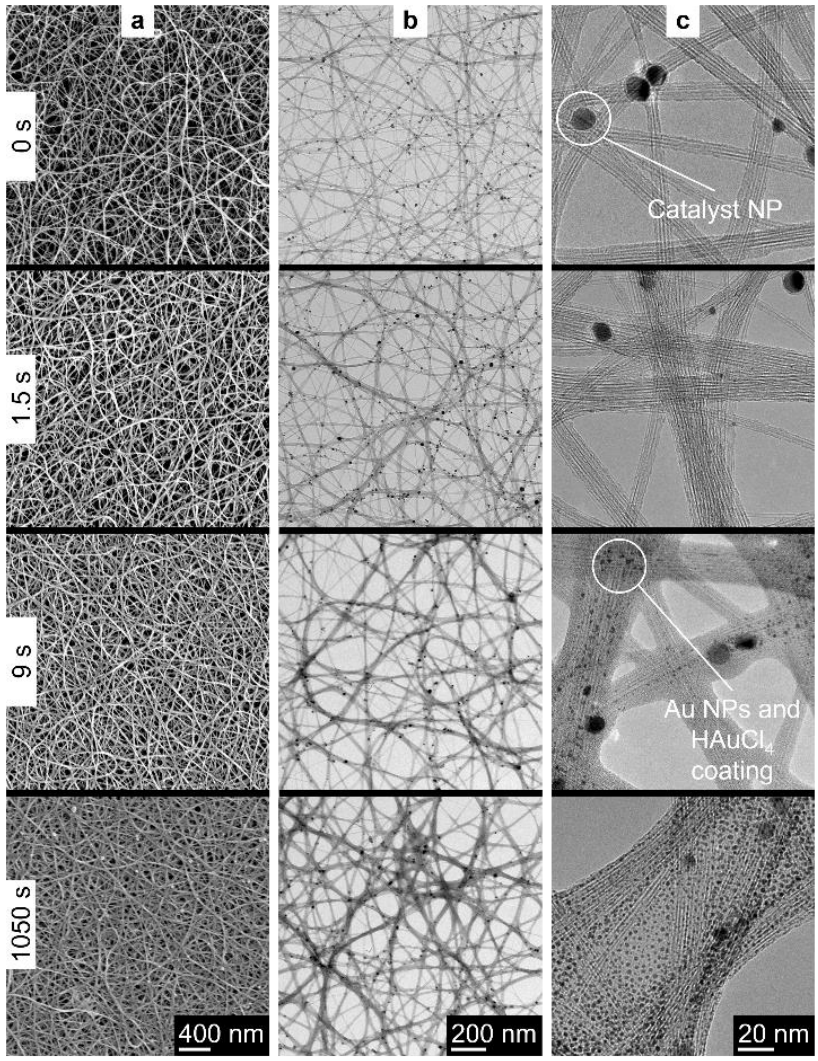

Figure 4.2.3-2. Typical (a) SEM and (b, c) TEM images of pristine (0.0 *s*) and doped SWCNTs at the doping time of 1.5, 9.0, and 1050 *s*. White circles indicate large and small black spots corresponding to catalyst and Au NPs.

To gain a detailed insight into the transformation of optical absorbance spectra under the doping and to correlate it, thereby, with the E_F position, we performed peak fitting for the spectra of pristine and doped SWCNT samples (Figure 4.2.3-3b-e). The experimental data were fitted with a model based on a linear combination of Lorentzian contours and exponential decay as discussed in details in Publication II. As a result, in the case of pristine nanotubes, we clearly observe all vHs transitions in semiconducting nanotubes from E_{11}^S to E_{55}^S and in metallic SWCNTs from E_{11}^M to E_{44}^M (Figure 4.2.3-3a). For the highly doped sample (1050 *s*), the low energy transitions disappear, but three new peaks can be clearly distinguished at 230, 315, and 1318 *nm* (Figure 4.2.3-3b). The origin

of the newborn peak at a higher wavelength is attributed to the intersubband plasmon [46]. The peaks at 230 and 315 nm most likely plasmons of gold NPs (Figure S4 and S5 in Publication II) [103].

The work function of the doped SWCNTs can be calculated from the peak fitting of the absorbance spectra. As we deal with not a single-chirality sample but with a distribution of the SWCNTs on the diameter, the position values of E_F could be estimated in a certain range from the disappearance of vHs transitions. The work function of the pristine SWCNTs as previously measured by ultraviolet photoemission spectroscopy technique has been obtained to be $\Phi_{0.0} = 4.45 \pm 0.10\ eV$ [103]. In principle, the E_F position in SWCNTs in air laboratory conditions can be shifted up to 0.7 eV [106,107] due to the ambient doping by oxygen. However, the annealing of the SWCNT film allowed us to recover the E_F to its intrinsic position. For the sample treated for 1.5 s, the work function is shifted to $\Phi_{1.5} = 4.82 \pm 0.15\ eV$. Indeed, we observe semiconducting E_{11}^S transition ($\Phi_{V1}^S = 4.71\ eV$) to disappear, while E_{22}^S transition ($\Phi_{V2}^S = 4.92\ eV$) is still present. At the doping time of 9.0 s, the work function can be estimated in line with the disappearance of E_{22}^S and still observable metallic E_{11}^M transition ($\Phi_{V1}^M = 5.15\ eV$): $\Phi_{9.0} = 5.03 \pm 0.15\ eV$. At 1050 s, we have no E_{11}^M and E_{33}^S ($\Phi_{V3}^S = 5.35\ eV$) transitions, but still observe E_{44}^S transition ($\Phi_{V4}^S = 5.57\ eV$) leading to $\Phi_{1050} = 5.46 \pm 0.15\ eV$.

For the clarity of the picture, we plot the vHs transitions with a corresponding shift of E_F in the DOS of typical 2 nm in diameter semiconducting and metallic nanotubes (Figure 4.2.3-3f) calculated within the third nearest neighbor tight-binding model [108]. While the doping time and a corresponding amount of the dopant increase, the vHs disappear one by one (Figure 4.2.3-3a,f). All this combined allowed us to estimate the work functions of the doped SWCNTs.

Additionally, the aerosol doping technique can be applied for SWCNT films with different thicknesses. However, in this case, the deposition parameters must be subsequently adjusted. To improve the control of the doping level in the case of thinner films ($T_{550} = 85\%$), we diluted the dopant concentration by a factor of two. This resulted in a 13.5-fold decrease of R_S: from 485 to 36 $\Omega/\square$. For thinner SWCNT films we observe similar behaviour with the disappearance of low energy peaks and appearance of the new plasmon peaks.

Apparently, the method we introduced can be easily applied to bendable and elastic substrates broadening, thereby, the range of applications of the developed TCFs to the field of flexible and stretchable devices [109]. The demonstrated method may be also applied to other low dimensional materials as well as their hybrid structures. These can yield numerous applications such as direct film micro-patterning, including drawing conductive paths for wiring,

and stack assembly for the creation of multi-layered functional materials [96,110,111].

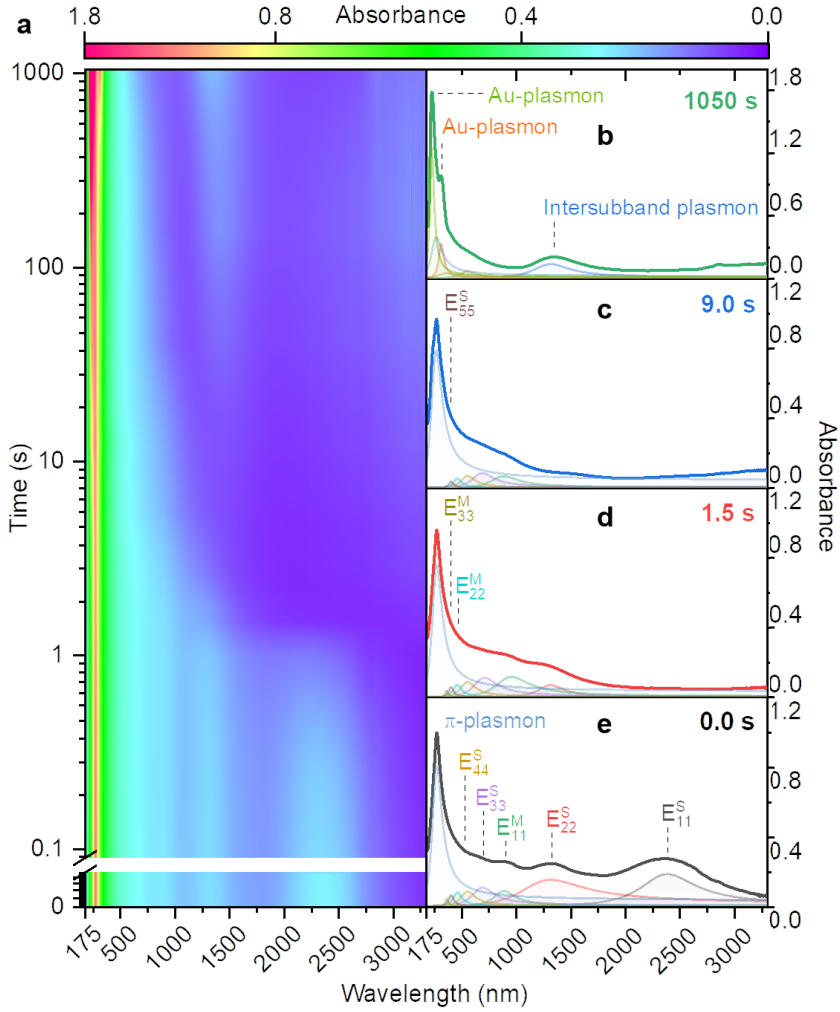

Figure 4.2.3-3. (a) UV-Vis-NIR absorbance color map and corresponding absorbance spectra of the T_{550} = 50% samples (with fitted peaks) at different doping times: (b) 1050, (c) 9.0, (d) 1.5, (e) 0.0 *s*. *The figure is continued on the next page.*

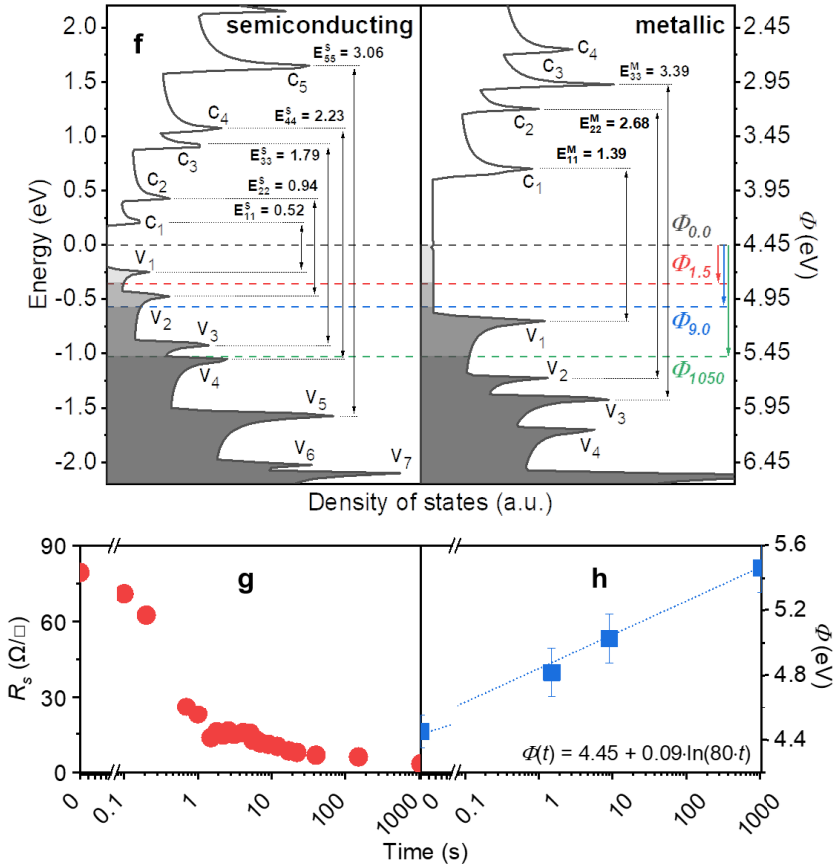

Figure 4.2.3-3. (f) DOS of (20,9) semi-conducting (left) and (25,1) metallic (right) SWCNTs and corresponding to the different doping times work function and E_F positions: 1050 (green), 9.0 (blue), 1.5 (red), 0.0 *s* (black). The time dependence of the optoelectronic characteristics during the doping: (g) sheet resistance R_S and (h) work function Φ. *The figure is continued from the previous page.*

5. Conclusions

In order to improve the optoelectronic performance of randomly oriented SWCNT films, several approaches are proposed. The first one introduces the fabrication procedure of a hybrid SWCNT/graphene material, which involves dry deposition of the SWCNT film onto a substrate, spray deposition of GO with its subsequent thermal reduction, and, finally, the doping procedure. Two methods for thermal reduction of GO are examined: ambient atmosphere reduction and H_2 reduction. It is shown that H_2 reduction is a more efficient method for removing oxygen-containing functional groups and, therefore, for a higher degree of GO reduction. However, absorption doping has a stronger effect on samples that are reduced at ambient atmosphere, since the doping is more susceptible to unrepaired structural defects. This process yields hybrid films with the equivalent sheet resistance as low as $R_{90} = 73\ \Omega/\square$.

The second approach uses several model dopant solvents to experimentally evaluate the influence of their nature on the resulted optoelectronic performance of doped SWCNT films. From the dependence of R_{90} on the solvent boiling point and its relation to the dispersive component of Hansen solubility theory it is concluded that the most significant factor in the doping process is the solvent evaporation rate. As a consequence, the lowest value of $R_{90} = 40\ \Omega/\square$ is measured for SWCNT films doped with $HAuCl_4$ dissolved in ethanol. For solvents with a higher boiling point, we optimized the overall film resistance by adjusting the temperature at which the doping is carried out. The samples produced in this work showed superior performance along with better stability values compared to the reported before.

The third approach based on an aerosol-assisted technique offers uniform, controllable and reproducible doping of SWCNT films. This method allows to fine-tune the work function and conductivity of the nanotubes by varying the time of deposition of liquid aerosol particles containing the dopant dissolved in ethanol. As a result, we controllably modulated the work function of pristine films with $T_{550} = 50\%$ in the range of $4.45 \div 5.46\ eV$. The corresponding sheet resistance of the highly doped SWCNT film is found to be as low as $3.2\ \Omega/\square$. For the films with $T_{550} = 85\%$ the sheet resistance dropped from 485 to $36\ \Omega/\square$.

In addition, the measurements of the broad wavelength spectra of complex conductance of a set of pristine and doped SWCNT films are carried out to

explain their THz-IR electrodynamic response. The main influence is attributed to unbound charge carriers which provide three main contributions. The first one is for delocalized carriers described by the Drude conductivity model. The next one is related to the weak resonance-like absorption band of around 100 μm (100 cm^{-1}) connected with plasmonic oscillations of carriers localized by intersections of SWCNTs in films. The third contribution is a gap-like feature on/less 1 mm (10 cm^{-1}) caused by tunnel barriers experienced by carriers at SWCNT contacts. To determine the THz-IR optical response, the effective parameters of the charge carriers (mobility, scattering rate, and mean-free path) were estimated based on the measured spectra. Also, along with the THz-IR response, the transient transport dynamics of photo-excited carriers in SWCNT films is discussed. Optical pump and THz probe spectroscopy reveals negative THz photoconductivity for both pristine and doped films. At the same time, the introduction of the doping decreases the photoconductivity, while the equilibrium conductivity increases. This means that the higher the concentration of free charge carriers, the lower the negative photoconductivity. One of the explanations is related to the existence of bound states for charge carriers, which lower the contribution to free charge carriers.

To sum-up, the studied optical and electrical characteristics in combination with novel post-synthesis approaches are presented to enhance the optoelectronic performance of randomly oriented SWCNT films. The fabricated films possess superior performance and satisfy most of the TCF requirements, which eventually can lead to completely free-form electrode designs as requested by numerous multi-functional applications.

References

[1] S. Iijima, Helical microtubules of graphitic carbon, Nature. 354 (1991) 56–58. doi:10.1038/354056a0.

[2] S. Iijima, T. Ichihashi, Single-shell carbon nanotubes of 1-nm diameter, Nature. 363 (1993) 603–605. doi:10.1038/363603a0.

[3] H. Kataura, Y. Kumazawa, Y. Maniwa, I. Umezu, S. Suzuki, Y. Ohtsuka, Y. Achiba, Optical properties of single-wall carbon nanotubes, Synth. Met. 103 (1999) 2555–2558. doi:10.1016/S0379-6779(98)00278-1.

[4] Y. Miyauchi, Photoluminescence studies on exciton photophysics in carbon nanotubes, J. Mater. Chem. C. 1 (2013) 6499. doi:10.1039/c3tc00947e.

[5] M.S. Dresselhaus, G. Dresselhaus, R. Saito, A. Jorio, Exciton Photophysics of Carbon Nanotubes, Annu. Rev. Phys. Chem. 58 (2007) 719–747. doi:10.1146/annurev.physchem.58.032806.104628.

[6] A. Jorio, R. Saito, G. Dresselhaus, M.S. Dresselhaus, Determination of nanotubes properties by Raman spectroscopy, Philos. Trans. R. Soc. London. Ser. A Math. Phys. Eng. Sci. 362 (2004) 2311–2336. doi:10.1098/rsta.2004.1443.

[7] A.G. Nasibulin, A. Moisala, D.P. Brown, H. Jiang, E.I. Kauppinen, A novel aerosol method for single walled carbon nanotube synthesis, Chem. Phys. Lett. 402 (2005) 227–232. doi:10.1016/J.CPLETT.2004.12.040.

[8] A. Moisala, A.G. Nasibulin, D.P. Brown, H. Jiang, L. Khriachtchev, E.I. Kauppinen, Single-walled carbon nanotube synthesis using ferrocene and iron pentacarbonyl in a laminar flow reactor, Chem. Eng. Sci. 61 (2006) 4393–4402. doi:10.1016/j.ces.2006.02.020.

[9] H. Ni, J. Liu, Z. Wang, S. Yang, A review on colorless and optically transparent polyimide films: Chemistry, process and engineering applications, J. Ind. Eng. Chem. 28 (2015) 16–27. doi:10.1016/J.JIEC.2015.03.013.

[10] M. Hasegawa, Development of Solution-Processable, Optically Transparent Polyimides with Ultra-Low Linear Coefficients of Thermal Expansion., Polymers (Basel). 9 (2017). doi:10.3390/polym9100520.

[11] S. Jewell, S.M. Kimball, Mineral Commodity Summaries, 2016. doi:10.3133/70202434.

[12] U.S. Geological Survey, MINERAL COMMODITY SUMMARIES 2019, 2019. doi:10.1007/978-3-540-47108-0-4.

[13] J. Park, B.G. Hyun, B.W. An, H.-G. Im, Y.-G. Park, J. Jang, J.-U. Park, B.-S. Bae, Flexible Transparent Conductive Films with High Performance and Reliability Using Hybrid Structures of Continuous Metal Nanofiber Networks for Flexible Optoelectronics, ACS Appl. Mater. Interfaces. 9 (2017) 20299–20305. doi:10.1021/acsami.7b04314.

[14] K.-H. Choi, H.-J. Nam, J.-A. Jeong, S.-W. Cho, H.-K. Kim, J.-W. Kang, D.-G. Kim, W.-J. Cho, Highly flexible and transparent InZnSnOx/Ag/InZnSnOx multilayer electrode for flexible organic light emitting diodes, Appl. Phys. Lett. 92 (2008) 223302. doi:10.1063/1.2937845.

[15] G. Gustafsson, Y. Cao, G.M. Treacy, F. Klavetter, N. Colaneri, A.J. Heeger, Flexible light-emitting diodes made from soluble conducting polymers, Nature. 357 (1992) 477–479. doi:10.1038/357477a0.

[16] I. Khrapach, F. Withers, T.H. Bointon, D.K. Polyushkin, W.L. Barnes, S. Russo, M.F. Craciun, Novel highly conductive and transparent graphene-based conductors, Adv. Mater. 24 (2012) 2844–2849. doi:10.1002/adma.201200489.

[17] D.S. Hecht, A.M. Heintz, R. Lee, L. Hu, B. Moore, C. Cucksey, S. Risser, High conductivity transparent carbon nanotube films deposited from superacid, Nanotechnology. 22 (2011) 075201. doi:10.1088/0957-4484/22/7/075201.

[18] I. V. Anoshkin, A.G. Nasibulin, Y. Tian, B. Liu, H. Jiang, E.I. Kauppinen, Hybrid carbon source for single-walled carbon nanotube synthesis by aerosol CVD method, Carbon N. Y. 78 (2014) 130–136. doi:10.1016/j.carbon.2014.06.057.

[19] A. Kaskela, A.G. Nasibulin, M.Y. Timmermans, B. Aitchison, A. Papadimitratos,

Y. Tian, Z. Zhu, H. Jiang, D.P. Brown, A. Zakhidov, E.I. Kauppinen, Aerosol-synthesized SWCNT networks with tunable conductivity and transparency by a dry transfer technique, Nano Lett. 10 (2010) 4349–4355. doi:10.1021/nl101680s.
[20] A.G. Nasibulin, A. Kaskela, K. Mustonen, A.S. Anisimov, V. Ruiz, S. Kivistö, S. Rackauskas, M.Y. Timmermans, M. Pudas, B. Aitchison, M. Kauppinen, D.P. Brown, O.G. Okhotnikov, E.I. Kauppinen, Multifunctional free-standing single-walled carbon nanotube films, ACS Nano. 5 (2011) 3214–3221. doi:10.1021/nn200338r.
[21] K. Mustonen, P. Laiho, A. Kaskela, T. Susi, A.G. Nasibulin, E.I. Kauppinen, Uncovering the ultimate performance of single-walled carbon nanotube films as transparent conductors, Appl. Phys. Lett. 107 (2015) 143113. doi:10.1063/1.4932942.
[22] Y. Liao, A. Hussain, P. Laiho, Q. Zhang, Y. Tian, N. Wei, E. Ding, S.A. Khan, N.N. Nguyen, S. Ahmad, E.I. Kauppinen, Tuning Geometry of SWCNTs by CO_2 in Floating Catalyst CVD for High-Performance Transparent Conductive Films, Adv. Mater. Interfaces. 5 (2018) 1801209. doi:10.1002/admi.201801209.
[23] A.S. Anisimov, A.G. Nasibulin, H. Jiang, P. Launois, J. Cambedouzou, S.D. Shandakov, E.I. Kauppinen, Mechanistic investigations of single-walled carbon nanotube synthesis by ferrocene vapor decomposition in carbon monoxide, Carbon N. Y. 48 (2010) 380–388. doi:10.1016/j.carbon.2009.09.040.
[24] V. Perebeinos, J. Tersoff, P. Avouris, Scaling of Excitons in Carbon Nanotubes, Phys. Rev. Lett. 92 (2004) 257402. doi:10.1103/PhysRevLett.92.257402.
[25] J. Jiang, R. Saito, G.G. Samsonidze, A. Jorio, S.G. Chou, G. Dresselhaus, M.S. Dresselhaus, Chirality dependence of exciton effects in single-wall carbon nanotubes: Tight-binding model, Phys. Rev. B. 75 (2007) 035407. doi:10.1103/PhysRevB.75.035407.
[26] K. An, Y. Lee, Electronic-structure engineering of carbon nanotubes, Nano. 1 (2006) 115–138. doi:10.1142/S1793292006000136.
[27] C. Biswas, Y.H. Lee, Graphene versus carbon nanotubes in electronic devices, Adv. Funct. Mater. 21 (2011) 3806–3826. doi:10.1002/adfm.201101241.
[28] D.L. Duong, I.H. Lee, K.K. Kim, J. Kong, S.M. Lee, Y.H. Lee, Carbon nanotube doping mechanism in a salt solution and hygroscopic effect: Density functional theory, ACS Nano. 4 (2010) 5430–5436. doi:10.1021/nn1011489.
[29] M. V. Kharlamova, Advances in tailoring the electronic properties of single-walled carbon nanotubes, Prog. Mater. Sci. 77 (2016) 125–211. doi:10.1016/j.pmatsci.2015.09.001.
[30] A. Murat, I. Rungger, C. Jin, S. Sanvito, U. Schwingenschlögl, Origin of the p-Type Character of AuCl 3 Functionalized Carbon Nanotubes, J. Phys. Chem. C. 118 (2014) 3319–3323. doi:10.1021/jp4100153.
[31] S.M. Kim, K.K. Kim, Y.W. Jo, M.H. Park, S.J. Chae, D.L. Duong, K.I.M.E.T. Al, Role of Anions in the AuCl 3 -Doping of Carbon Nanotubes, ACS Nano. (2011) 1236–1242. doi:10.1021/nn1028532.
[32] I.H. Lee, U.J. Kim, H. Bin Son, S.-M. Yoon, F. Yao, W.J. Yu, D.L. Duong, J.-Y. Choi, J.M. Kim, E.H. Lee, Y.H. Lee, Hygroscopic Effects on AuCl 3 -Doped Carbon Nanotubes, J. Phys. Chem. C. 114 (2010) 11618–11622. doi:10.1021/jp1036662.
[33] K.K. Kim, J.J. Bae, H.K. Park, S.M. Kim, H.-Z. Geng, K.A. Park, H.-J. Shin, S.-M. Yoon, A. Benayad, J.-Y. Choi, Y.H. Lee, Fermi Level Engineering of Single-Walled Carbon Nanotubes by $AuCl_3$ Doping, J. Am. Chem. Soc. 130 (2008) 12757–12761. doi:10.1021/ja8038689.
[34] S.M. Kim, K.K. Kim, D.L. Duong, Y. Hirana, Y. Tanaka, Y. Niidome, N. Nakashima, J. Kong, Y.H. Lee, Spectroscopic determination of the electrochemical potentials of n-type doped carbon nanotubes, J. Phys. Chem. C. 116 (2012) 5444–5449. doi:10.1021/jp211583t.
[35] K.K. Kim, S.M. Kim, Y.H. Lee, Chemically Conjugated Carbon Nanotubes and Graphene for Carrier Modulation, Acc. Chem. Res. 49 (2016) 390–399. doi:10.1021/acs.accounts.5b00441.
[36] Y. Tanaka, Y. Hirana, Y. Niidome, K. Kato, S. Saito, N. Nakashima, Experimentally determined redox potentials of individual (n,m) single-walled carbon nanotubes, Angew. Chemie - Int. Ed. (2009). doi:10.1002/anie.200902468.
[37] D. Paolucci, M.M. Franco, M. Iurlo, M. Marcaccio, M. Prato, F. Zerbetto, A.

Pénicaud, F. Paolucci, Singling out the electrochemistry of individual single-walled carbon nanotubes in solution, J. Am. Chem. Soc. (2008). doi:10.1021/ja710625p.
[38] S.M. Kim, J.H. Jang, K.K. Kim, H.K. Park, J.J. Bae, W.J. Yu, H. Lee, G. Kim, D.D. Loc, U.J. Kim, E.H. Lee, H.J. Shin, J.Y. Choi, Y.H. Lee, Reduction-controlled viologen in bisolvent as an environmentally stable n-type dopant for carbon nanotubes, J. Am. Chem. Soc. (2009). doi:10.1021/ja807480g.
[39] B.R. Kang, W.J. Yu, K.K. Kim, H.K. Park, S.M. Kim, Y. Park, C. Kim, H.J. Shin, U. Kim, E.H. Lee, J.Y. Choi, Y.H. Lee, Restorable type conversion of carbon nanotube transistor using pyrolytically controlled antioxidizing photosynthesis coenzyme, Adv. Funct. Mater. (2009). doi:10.1002/adfm.200801712.
[40] K.K. Kim, S.-M. Yoon, H.K. Park, H.-J. Shin, S.M. Kim, J.J. Bae, Y. Cui, J.M. Kim, J.-Y. Choi, Y.H. Lee, Doping strategy of carbon nanotubes with redox chemistry, New J. Chem. 34 (2010) 2183. doi:10.1039/c0nj00138d.
[41] A.G. Marinopoulos, L. Wirtz, A. Marini, V. Olevano, A. Rubio, L. Reining, Optical absorption and electron energy loss spectra of carbon and boron nitride nanotubes: a first-principles approach, Appl. Phys. A. 78 (2004) 1157–1167. doi:10.1007/s00339-003-2467-z.
[42] M. Pfohl, D.D. Tune, A. Graf, J. Zaumseil, R. Krupke, B.S. Flavel, Fitting Single-Walled Carbon Nanotube Optical Spectra, ACS Omega. 2 (2017) 1163–1171. doi:10.1021/acsomega.6b00468.
[43] Z. Luo, L.D. Pfefferle, G.L. Haller, F. Papadimitrakopoulos, (n,m) abundance evaluation of single-walled carbon nanotubes by fluorescence and absorption spectroscopy, J. Am. Chem. Soc. 128 (2006) 15511–15516. doi:10.1021/ja0657096.
[44] A. V. Naumov, S. Ghosh, D.A. Tsyboulski, S.M. Bachilo, R.B. Weisman, Analyzing Absorption Backgrounds in Single-Walled Carbon Nanotube Spectra, ACS Nano. 5 (2011) 1639–1648. doi:10.1021/nn1035922.
[45] S. Ohmori, T. Saito, M. Tange, B. Shukla, T. Okazaki, M. Yumura, S. Iijima, Fundamental importance of background analysis in precise characterization of single-walled carbon nanotubes by optical absorption spectroscopy, J. Phys. Chem. C. 114 (2010) 10077–10081. doi:10.1021/jp9120172.
[46] D. Satco, A.R.T. Nugraha, M.S. Ukhtary, D. Kopylova, A.G. Nasibulin, R. Saito, Intersubband plasmon excitations in doped carbon nanotubes, Phys. Rev. B. 99 (2019) 075403. doi:10.1103/PhysRevB.99.075403.
[47] K. Sasaki, Y. Tokura, Theory of a Carbon-Nanotube Polarization Switch, (2017). doi:10.1103/PhysRevApplied.9.034018.
[48] A. Jorio, A.G. Souza Filho, Raman Studies of Carbon Nanostructures, Annu. Rev. Mater. Res. 46 (2016) 357–382. doi:10.1146/annurev-matsci-070115-032140.
[49] J. Maultzsch, H. Telg, S. Reich, C. Thomsen, Radial breathing mode of single-walled carbon nanotubes: Optical transition energies and chiral-index assignment, Phys. Rev. B - Condens. Matter Mater. Phys. 72 (2005). doi:10.1103/PhysRevB.72.205438.
[50] R.N. Gontijo, G.A.M. Sáfar, A. Righi, R.M. Jain, M.S. Strano, C. Fantini, Quantifying (n,m) species in single-wall carbon nanotubes dispersions by combining Raman and optical absorption spectroscopies, Carbon N. Y. 115 (2017) 681–687. doi:10.1016/j.carbon.2017.01.041.
[51] A. Jorio, A. Jorio, A.G. Souza Filho, A.G. Souza Filho, G. Dresselhaus, M.S. Dresselhaus, M.S. Dresselhaus, A.K. Swan, M.S. Ünlü, B.B. Goldberg, B.B. Goldberg, M.A. Pimenta, J.H. Hafner, C.M. Lieber, R. Saito, G-band resonant Raman study of 62 isolated single-wall carbon nanotubes, Phys. Rev. B - Condens. Matter Mater. Phys. 65 (2002) 1554121–1554129. doi:10.1103/PhysRevB.65.155412.
[52] J.E. Proctor, D. Melendrez Armada, A. Vijayaraghavan, An Introduction to Graphene and Carbon Nanotubes., CRC Press LLC, n.d. https://www.crcpress.com/An-Introduction-to-Graphene-and-Carbon-Nanotubes/Proctor-Armada-Vijayaraghavan/p/book/9781498751797 (accessed May 20, 2019).
[53] K. Mustonen, T. Susi, A.G. Nasibulin, H. Jiang, M. He, E.I. Kauppinen, Direct synthesis of high-quality single-walled carbon nanotubes by the physical nucleation of iron nanoparticles in an atmospheric pressure carbon monoxide flow, Carbon N. Y. 50 (2012) 5343–5345. doi:10.1016/j.carbon.2012.07.006.

[54] K. Mustonen, P. Laiho, A. Kaskela, Z. Zhu, O. Reynaud, N. Houbenov, Y. Tian, T. Susi, H. Jiang, A.G. Nasibulin, E.I. Kauppinen, Gas phase synthesis of non-bundled, small diameter single-walled carbon nanotubes with near-armchair chiralities, Appl. Phys. Lett. 107 (2015). doi:10.1063/1.4926415.
[55] K. Mustonen, T. Susi, A. Kaskela, P. Laiho, Y. Tian, A.G. Nasibulin, E.I. Kauppinen, Influence of the diameter of single-walled carbon nanotube bundles on the optoelectronic performance of dry-deposited thin films, Beilstein J. Nanotechnol. 3 (2012) 692–702. doi:10.3762/bjnano.3.79.
[56] D. Hecht, L. Hu, G. Grüner, Conductivity scaling with bundle length and diameter in single walled carbon nanotube networks, Appl. Phys. Lett. 89 (2006) 2004–2007. doi:10.1063/1.2356999.
[57] B.P. Gorshunov, E.S. Zhukova, J.S. Starovatykh, M.A. Belyanchikov, A.K. Grebenko, A. V. Bubis, V.I. Tsebro, A.A. Tonkikh, D. V. Rybkovskiy, A.G. Nasibulin, E.I. Kauppinen, E.D. Obraztsova, Terahertz spectroscopy of charge transport in films of pristine and doped single-wall carbon nanotubes, Carbon N. Y. (2018). doi:10.1016/j.carbon.2017.10.072.
[58] H. Xu, S.M. Anlage, L. Hu, G. Gruner, Microwave shielding of transparent and conducting single-walled carbon nanotube films, Appl. Phys. Lett. 90 (2007) 183119. doi:10.1063/1.2734897.
[59] O. Hilt, H.B. Brom, M. Ahlskog, Localized and delocalized charge transport in single-wall carbon-nanotube mats, Phys. Rev. B. 61 (2000) R5129–R5132. doi:10.1103/PhysRevB.61.R5129.
[60] V.I. Tsebro, A.A. Tonkikh, D. V. Rybkovskiy, E.A. Obraztsova, E.I. Kauppinen, E.D. Obraztsova, Phonon contribution to electrical resistance of acceptor-doped single-wall carbon nanotubes assembled into transparent films, Phys. Rev. B. (2016). doi:10.1103/PhysRevB.94.245438.
[61] M. V. Shuba, A.G. Paddubskaya, A.O. Plyushch, P.P. Kuzhir, G.Y. Slepyan, S.A. Maksimenko, V.K. Ksenevich, P. Buka, D. Seliuta, I. Kasalynas, J. MacUtkevic, G. Valusis, C. Thomsen, A. Lakhtakia, Experimental evidence of localized plasmon resonance in composite materials containing single-wall carbon nanotubes, Phys. Rev. B - Condens. Matter Mater. Phys. (2012). doi:10.1103/PhysRevB.85.165435.
[62] T. Nakanishi, T. Ando, Optical Response of Finite-Length Carbon Nanotubes, J. Phys. Soc. Japan. (2009). doi:10.1143/jpsj.78.114708.
[63] Q. Zhang, E.H. Hároz, Z. Jin, L. Ren, X. Wang, R.S. Arvidson, A. Lüttge, J. Kono, Plasmonic Nature of the Terahertz Conductivity Peak in Single-Wall Carbon Nanotubes, Nano Lett. 13 (2013) 5991–5996. doi:10.1021/nl403175g.
[64] M. V. Shuba, A.G. Paddubskaya, P.P. Kuzhir, G.Y. Slepyan, D. Seliuta, I. Kašalynas, G. Valušis, A. Lakhtakia, Effects of inclusion dimensions and p-type doping in the terahertz spectra of composite materials containing bundles of single-wall carbon nanotubes, J. Nanophotonics. 6 (2012) 061707. doi:10.1117/1.JNP.6.061707.
[65] A.B. Kaiser, Electronic transport properties of conducting polymers and carbon nanotubes, Reports Prog. Phys. (2001). doi:10.1088/0034-4885/64/1/201.
[66] L.C. Venema, J.W.G. Wildöer, J.W. Janssen, S.J. Tans, H.L.J. Temminck Tuinstra, L.P. Kouwenhoven, C. Dekker, Imaging electron wave functions of quantized energy levels in carbon nanotubes, Science (80-.). (1999). doi:10.1126/science.283.5398.52.
[67] J.T. Hong, D.J. Park, J.Y. Moon, S.B. Choi, J.K. Park, Farbian Rotermund, J.Y. Park, S. Lee, Y.H. Ahn, Terahertz wave applications of single-walled carbon nanotube films with high shielding effectiveness, Appl. Phys. Express. (2012). doi:10.1143/APEX.5.015102.
[68] J.Y. Park, S. Rosenblatt, Y. Yaish, V. Sazonova, H. Üstunel, S. Braig, T.A. Arias, P.W. Brouwer, P.L. McEuen, Electron-phonon scattering in metallic single-walled carbon nanotubes, Nano Lett. (2004). doi:10.1021/nl035258c.
[69] J.M. Marulanda, A. Srivastava, Carrier density and effective mass calculations in carbon nanotubes, in: Phys. Status Solidi Basic Res., 2008. doi:10.1002/pssb.200844259.
[70] G.M. Mikheev, A.G. Nasibulin, R.G. Zonov, A. Kaskela, E.I. Kauppinen, Photon-Drag Effect in Single-Walled Carbon Nanotube Films, Nano Lett. 12 (2012) 77–83. doi:10.1021/nl203003p.
[71] A.R. Amori, Z. Hou, T.D. Krauss, Excitons in Single-Walled Carbon Nanotubes and Their Dynamics, Annu. Rev. Phys. Chem. 69 (2018) 81–99.

doi:10.1146/annurev-physchem-050317-014241.
[72] C. Georgi, M. Böhmler, H. Qian, L. Novotny, A. Hartschuh, Probing exciton propagation and quenching in carbon nanotubes with near-field optical microscopy, Phys. Status Solidi Basic Res. (2009). doi:10.1002/pssb.200982306.
[73] S. Moritsubo, T. Murai, T. Shimada, Y. Murakami, S. Chiashi, S. Maruyama, Y.K. Kato, Exciton diffusion in air-suspended single-walled carbon nanotubes, Phys. Rev. Lett. (2010). doi:10.1103/PhysRevLett.104.247402.
[74] K. Yoshikawa, K. Matsuda, Y. Kanemitsu, Exciton transport in suspended single carbon nanotubes studied by photoluminescence imaging spectroscopy, J. Phys. Chem. C. (2010). doi:10.1021/jp911518h.
[75] R. Matsunaga, K. Matsuda, Y. Kanemitsu, Observation of charged excitons in hole-doped carbon nanotubes using photoluminescence and absorption spectroscopy, Phys. Rev. Lett. (2011). doi:10.1103/PhysRevLett.106.037404.
[76] H. Hartleb, F. Späth, T. Hertel, Evidence for Strong Electronic Correlations in the Spectra of Gate-Doped Single-Wall Carbon Nanotubes, ACS Nano. (2015). doi:10.1021/acsnano.5b04707.
[77] T. Nishihara, Y. Yamada, M. Okano, Y. Kanemitsu, Trion formation and recombination dynamics in hole-doped single-walled carbon nanotubes, Appl. Phys. Lett. (2013). doi:10.1063/1.4813014.
[78] M. Yoshida, A. Popert, Y.K. Kato, Gate-voltage induced trions in suspended carbon nanotubes, Phys. Rev. B. (2016). doi:10.1103/PhysRevB.93.041402.
[79] F. Taherian, V. Marcon, N.F.A. Van Der Vegt, F. Leroy, What is the contact angle of water on graphene?, Langmuir. (2013). doi:10.1021/la304645w.
[80] S. Bittolo Bon, L. Valentini, J.M. Kenny, L. Peponi, R. Verdejo, M.A. Lopez-Manchado, Electrodeposition of transparent and conducting graphene/carbon nanotube thin films, Phys. Status Solidi. 207 (2010) 2461–2466. doi:10.1002/pssa.201026138.
[81] I.N. Kholmanov, C.W. Magnuson, R. Piner, J.Y. Kim, A.E. Aliev, C. Tan, T.Y. Kim, A.A. Zakhidov, G. Sberveglieri, R.H. Baughman, R.S. Ruoff, Optical, electrical, and electromechanical properties of hybrid graphene/carbon nanotube films, Adv. Mater. 27 (2015) 3053–3059. doi:10.1002/adma.201500785.
[82] V.C. Tung, L.-M. Chen, M.J. Allen, J.K. Wassei, K. Nelson, R.B. Kaner, Y. Yang, Low-Temperature Solution Processing of Graphene–Carbon Nanotube Hybrid Materials for High-Performance Transparent Conductors, Nano Lett. 9 (2009) 1949–1955. doi:10.1021/nl9001525.
[83] J.H. Jang, S.C. Lim, D.L. Duong, G. Kim, W.J. Yu, K.H. Han, Y.-S. Min, Y.H. Lee, Doping of Carbon Nanotubes Using Low Energy Ion Implantation, J. Nanosci. Nanotechnol. 10 (2010) 3934–3939. doi:10.1166/jnn.2010.1989.
[84] P.J. Murphy, G. Stevens, M.S. Lagrange, The effects of temperature and pressure on gold-chloride speciation in hydrothermal fluids: A Raman spectroscopic study, Geochim. Cosmochim. Acta. 64 (2000) 479–494. doi:10.1016/S0016-7037(99)00293-8.
[85] D.R. Lide, CRC Handbook of Chemistry and Physics, 84th Edition, 2003-2004, Handb. Chem. Phys. 53 (2003) 2616. doi:10.1136/oem.53.7.504.
[86] M. Luo, Y. Liu, W. Huang, W. Qiao, Y. Zhou, Y. Ye, L. Sen Chen, Towards flexible transparent electrodes based on carbon and metallic materials, Micromachines. 8 (2017) 1–16. doi:10.3390/mi8010012.
[87] S.H. Chae, Y.H. Lee, Carbon nanotubes and graphene towards soft electronics, Nano Converg. 1 (2014) 15. doi:10.1186/s40580-014-0015-5.
[88] L. He, S.C. Tjong, Nanostructured transparent conductive films: Fabrication, characterization and applications, Mater. Sci. Eng. R Reports. 109 (2016) 1–101. doi:10.1016/j.mser.2016.08.002.
[89] L. Hu, D.S. Hecht, G. Grüner, Carbon Nanotube Thin Films: Fabrication, Properties, and Applications, Chem. Rev. 110 (2010) 5790–5844. doi:10.1021/cr9002962.
[90] L. Yu, C. Shearer, J. Shapter, Recent Development of Carbon Nanotube Transparent Conductive Films, Chem. Rev. 116 (2016) 13413–13453. doi:10.1021/acs.chemrev.6b00179.
[91] Y. Zhou, R. Azumi, Carbon nanotube based transparent conductive films: progress, challenges, and perspectives, Sci. Technol. Adv. Mater. 17 (2016) 493–516. doi:10.1080/14686996.2016.1214526.

[92] N.T.K. Thanh, N. Maclean, S. Mahiddine, Mechanisms of nucleation and growth of nanoparticles in solution, Chem. Rev. 114 (2014) 7610–7630. doi:10.1021/cr400544s.
[93] P.. Murphy, M.. LaGrange, Raman spectroscopy of gold chloro-hydroxy speciation in fluids at ambient temperature and pressure: a re-evaluation of the effects of pH and chloride concentration, Geochim. Cosmochim. Acta. 62 (1998) 3515–3526. doi:10.1016/S0016-7037(98)00246-4.
[94] H. Yun, S. Kim, Stabilization of gold doped single-walled carbon nanotube film by electropolymerization, Appl. Phys. Lett. 101 (2012). doi:10.1063/1.4745198.
[95] S.D. Bergin, Z. Sun, D. Rickard, P. V. Streich, J.P. Hamilton, J.N. Coleman, Multicomponent solubility parameters for single-walled carbon nanotube-solvent mixtures, ACS Nano. 3 (2009) 2340–2350. doi:10.1021/nn900493u.
[96] Q. Zhang, L.F. Tan, Y.X. Chen, T. Zhang, W.J. Wang, Z. Liu, L. Fu, Human-like sensing and reflexes of graphene-based films, Adv. Sci. 3 (2016). doi:10.1002/advs.201600130.
[97] S.D. Shandakov, M. V. Lomakin, A.G. Nasibulin, The effect of the environment on the electronic properties of single-walled carbon nanotubes, Tech. Phys. Lett. 42 (2016) 1071–1075. doi:10.1134/S1063785016110080.
[98] V. Derycke, R. Martel, J. Appenzeller, P. Avouris, Controlling doping and carrier injection in carbon nanotube transistors, Appl. Phys. Lett. 80 (2002) 2773–2775. doi:10.1063/1.1467702.
[99] H.-Z. Geng, K.K. Kim, K.P. So, Y.S. Lee, Y. Chang, Y.H. Lee, Effect of Acid Treatment on Carbon Nanotube-Based Flexible Transparent Conducting Films, J. Am. Chem. Soc. 129 (2007) 7758–7759. doi:10.1021/ja0722224.
[100] Z. Wu, Transparent, Conductive Carbon Nanotube Films, Science (80-.). 305 (2004) 1273–1276. doi:10.1126/science.1101243.
[101] J. Zhang, M. Terrones, C.R. Park, R. Mukherjee, M. Monthioux, N. Koratkar, Y.S. Kim, R. Hurt, E. Frackowiak, T. Enoki, Y. Chen, Y. Chen, A. Bianco, Carbon science in 2016: Status, challenges and perspectives, Carbon N. Y. 98 (2016) 708–732. doi:10.1016/j.carbon.2015.11.060.
[102] D. Shim, S.H. Jung, S.Y. Han, K. Shin, K.H. Lee, J.H. Han, Improvement of SWCNT transparent conductive films via transition metal doping, Chem. Commun. (2011). doi:10.1039/c1cc10190k.
[103] A.P. Tsapenko, A.E. Goldt, E. Shulga, Z.I. Popov, K.I. Maslakov, A.S. Anisimov, P.B. Sorokin, A.G. Nasibulin, Highly conductive and transparent films of HAuCl4-doped single-walled carbon nanotubes for flexible applications, Carbon N. Y. 130 (2018) 448–457. doi:10.1016/J.CARBON.2018.01.016.
[104] P. Kulkarni, P.A. Baron, K. Willeke, Aerosol Measurement: Principles, Techniques, and Applications: Third Edition, 2011. doi:10.1002/9781118001684.
[105] I. Agranovski, Aerosols - Science and Technology, 2010. doi:10.1002/9783527630134.
[106] K.K. Kim, J.J. Bae, H.K. Park, S.M. Kim, H.-Z. Geng, K.A. Park, H.-J. Shin, S.-M. Yoon, A. Benayad, J.-Y. Choi, Y.H. Lee, Fermi level engineering of single-walled carbon nanotubes by AuCl3 doping., J. Am. Chem. Soc. 130 (2008) 12757–12761. doi:10.1021/ja8038689.
[107] S.D. Shandakov, M. V. Lomakin, A.G. Nasibulin, The effect of the environment on the electronic properties of single-walled carbon nanotubes, Tech. Phys. Lett. 42 (2016) 1071–1075. doi:10.1134/S1063785016110080.
[108] R. Chegel, Third-Nearest-Neighbors Tight-Binding Description of Optical Response of Carbon Nanotubes: Effects of Chirality and Diameter, J. Electron. Mater. 44 (2015) 3500–3511. doi:10.1007/s11664-015-3877-3.
[109] E.P. Gilshteyn, S. Lin, V.A. Kondrashov, D.S. Kopylova, A.P. Tsapenko, A.S. Anisimov, A.J. Hart, X. Zhao, A.G. Nasibulin, A One-Step Method of Hydrogel Modification by Single-Walled Carbon Nanotubes for Highly Stretchable and Transparent Electronics, ACS Appl. Mater. Interfaces. 10 (2018) 28069–28075. doi:10.1021/acsami.8b08409.
[110] X. Wang, Z. Liu, T. Zhang, Flexible Sensing Electronics for Wearable/Attachable Health Monitoring, Small. 13 (2017). doi:10.1002/smll.201602790.
[111] D.L. Duong, S.J. Yun, Y.H. Lee, van der Waals Layered Materials: Opportunities and Challenges, ACS Nano. 11 (2017) 11803–11830. doi:10.1021/acsnano.7b07436.

Randomly oriented single-walled carbon nanotube (SWCNT) films being one of the most rapidly evolving material for numerous applications in transparent conductors provide both unprecedented flexibility and stretchability. At the same time, their low resistance at high transmittance values in the visible spectrum still limits their wide usage.

The thesis introduces approaches to improve the optoelectronic characteristics of the films by means of adsorption doping technique. The proposed methods lead to state-of-the-art values by creation of a hybrid material, use of solvent optimization procedure, and fine-tuning of the optical and electrical parameters of SWCNT films. This opens a new avenue for traditional and flexible optoelectronics both to replace existing metal-oxide electrodes and to develop novel applications for highly transparent and conductive films.

Aalto-DD 176/2019

ISBN 978-952-60-8737-5 (printed)
ISBN 978-952-60-8738-2 (pdf)
ISSN 1799-4934 (printed)
ISSN 1799-4942 (pdf)

Aalto University
School of Science
Department of Applied Physics
www.aalto.fi

BUSINESS + ECONOMY

ART + DESIGN + ARCHITECTURE

SCIENCE + TECHNOLOGY

CROSSOVER

DOCTORAL DISSERTATIONS